Imaging Regional Geology and Au – Sulphide mineralization over Dhanjori greenstone belt: Implications from 3-D Inversion of Audio Magnetotelluric data and Petrophysical Characterization

Roshan K. Singh[a], Ved P. Maurya[b], Shalivahan[a,*], Sahendra Singh[c]

[a] *Department of Applied Geophysics, IIT (ISM), Dhanbad 826004, India*
[b] *Observatório Nacional, Rua General José Cristino, 77, Rio de Janeiro, RJ 20921-400, Brazil*
[c] *Department of Applied Geology, IIT (ISM), Dhanbad 826004, India*

ABSTRACT

The 2.1-Ga-old Paleoproterozoic Dhanjori Group of rocks covers 800 sq. km area within the Singhbhum Crustal province of eastern India, and is composed of siliciclastic metasedimentary sequence interlayered with mafic to ultramafic rocks. The meta-volcanosedimentary sequence is deformed and is of low-grade greenschist metamorphic facies. The gold occurrences within the study area are confined to the sulphide hosted mafic/ultramafic volcanic rocks and also in the basal quartz pebble conglomerates (QPC) within the Dhanjori Formation. Gold mineralization within the mafic/ultramafic meta-volcanics formations occurs within the quartz $\pm$ carbonate vein i.e. lode gold and as detrital gold within the QPC ($0.5 - 7$ ppm) of Phuljhari Formations. Regional Audio Magnetotelluric (AMT) measurements across the geological domains of Dhanjori Group and Iron Ore Group (IOG) were carried out in the frequency range of 10 kHz–10 Hz. This work discusses the conductivity model from 3-D inversion along with geology and petrophysical properties in mapping the regional geological features, associated sulphide mineralization and influence of texture, grain and bulk properties on mineralization. Dimensionality and strike analysis of the AMT data indicate complex conductivity structures. 3-D inversion of off-diagonal component of impedance was performed for obtaining an optimum value of uniform half space initial resistivity and error floor for off-diagonal component of impedance data. These were used to perform 3-D inversion of full impedance to produce a conductivity model of the study area. The conductivity model delineated major geological boundaries and the sulphide bearing mineralized zone. A major conductor is observed which extends to a depth of ~ 250 m within meta-volcanics. On comparison with the available borehole adjacent to this, it is confirmed that the conductor corresponds to sulphide mineralization. The resistivity low at a depth of 150 m coincides with metabasalts (pyrite present which extends to 159 m with arsenopyrite). Another mineralized zone is observed at the boundary of iron ore group volcanics and Proterozoic-gabbro-anorthosite-ultramafics (PGAU), it starts appearing from a depth of ~ 400 m and can be seen which extends to a depth of ~ 800 m. It is worth mentioning that there lies Kundarkocha gold mine in the same geological domain. In addition, near surface conductor to a maximum depth of ~ 50 m is observed all along the AMT profile. The sediments and fluids could account for this conducting feature. This is in agreement with available Electrical Resistivity Tomography section. The borehole within Dhanjori Volcanics also detected sulphide mineralization for ~ 50 m. Thus, it can be inferred that the near surface conductor indicates the presence of gold in association with other sulphide minerals. The petrophysical studies helped to estimate the concentration of minerals within the rocks. High density and low susceptibilities in the area is an indicative of low-grade metamorphism and low level of serpentenization. Combined density and susceptibility scatter diagram and component proportion phase diagram suggests 20 vol%, 78 vol% and 2 vol% of haematite/sulphides, barren rocks and magnetite respectively. The high value of chargeability and negligible value of susceptibility indicates the presence of disseminated sulphides rather than haematites and/or massive sulphides in the rocks. Ternary plot suggest that the mineralization is controlled by texture and grain properties. Petrophysical analysis suggests that the lithotypes of the study area are similar to those of greenstone terrain in the Abitibi Subprovince. Integrating inverted section, geology and petrophysical properties has a substantial impact on the study area in terms of predicting the mineralization prospect and at the same time substantially reduces the drilling cost. Thus, the study provides a new orientation and advancement to the exploration strategy for deeper deposits.

1. Introduction

Magnetotelluric (MT)/Audio Magnetotelluric (AMT) is a natural source electromagnetic technique suitably used to map shallow subsurface conductivity distribution from few tens of meters to several kilometres. Numerous MT/AMT studies have been conducted over mineral occurrences of the world (Koziar and Strangway, 1978, Livelybrooks et al., 1996; Meju, 2002; Jones and Garcia 2003; Heinson et al., 2006; Tuncer et al., 2006; Queralt et al., 2007, Yamaguchi et al., 2010, Craven et al., 2013). Greenstone belts host most of the well-known gold deposits (Groves et al., 1987) with associated minerals such as silver, copper, zinc, nickel and lead (Pirajno, 2007). Some of the greenstone belts of India are Chitradurga greenstone belt, Sargur group Nagamangala greenstone belts, part of Western Dharwar, and Kadiri
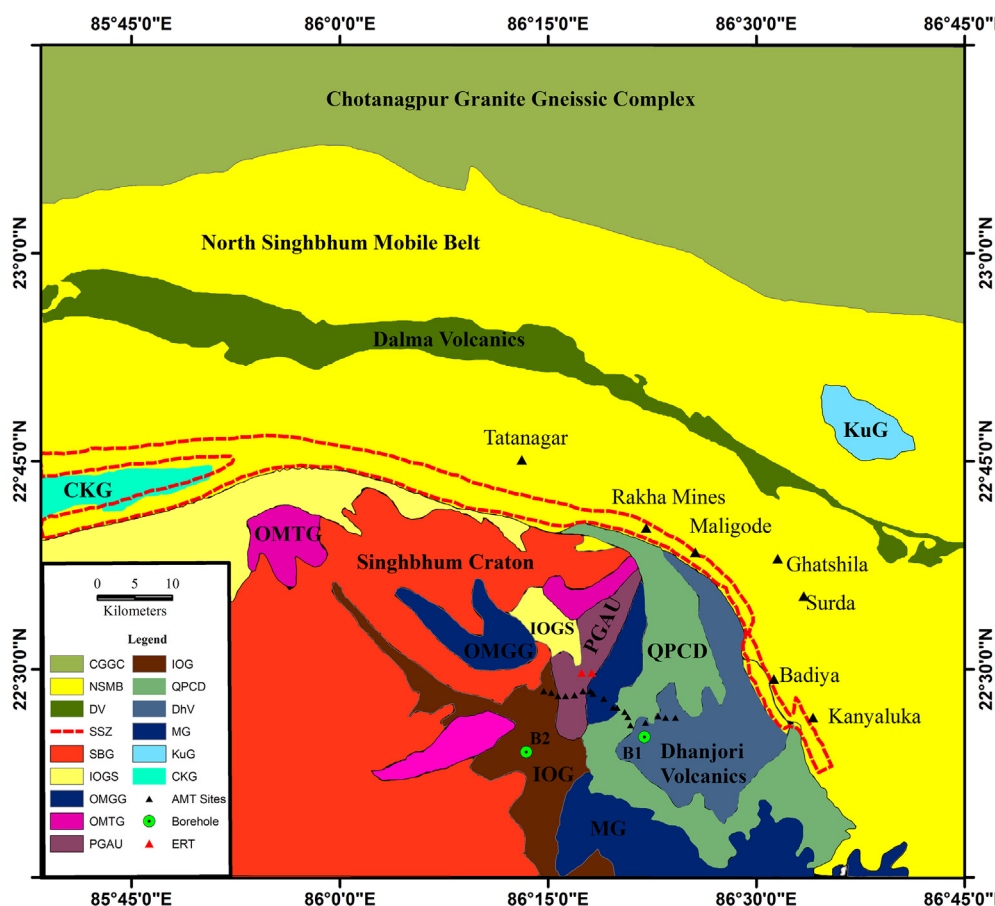

Fig. 1a. Geological map showing the distribution of stratigraphic units in parts of eastern India after Saha (1994): where CGGC is Chotanagpur Granite Gneissic Complex; NSMB is North Singhbhum Granite Complex; DV is Dalma Volcanics; SSZ is Singhbhum Shear Zone ; IOGS is Iron Ore Group shale, tuff and phyllite; OMGG is Older Metamorphic Group Granite; OMTG is Older Metamorphic Tonalitic Gneiss; PGAU is Proterozoic-Gabbro-Anorthosite-Ultramafics; IOG is Iron Ore Group volcanics; DhV is Dhanjori Volcanics; MG is Mayurbhanj Granite; KuG is Kuilapal Granite; CKG is Chakradharpur Granite; Black closed triangles are AMT sites.

greenstone belts, part of Eastern Dharwar Supergroup (Jayananda et al., 2013) and Dhanjori Volcanics (DhV). The Dhanjori volcanism took place in an intracontinental rift setting (Eriksson et al., 1999; Mazumder et al., 2000; Mazumder, 2002, 2003). DhV lies at the eastern part of the Singhbum Craton (Fig. 1a), of the Eastern Indian Craton (EIC) and is mainly characterized by the Archean nucleus of Singhbhum Granite (SG) batholithic complex and ancient supracrustals surrounded by several elongate and arcuate Proterozoic belts (Saha, 1994). It is one of oldest among the five large early Proterozoic mafic volcanic suites of the Singhbhum Craton (Saha, 1994). DhV shows evidences of gold and other economic minerals (Haque and Dutta, 1996; Mazumder, 2005; Deb, 2014). The greenstone belt of DhV shows similar characteristics likewise Dharwar gold prospects of southern India, Barberton in South Africa, Yilgarn craton of Australia, and Abitibi greenstone belt of Canada. Greenstone belt consists of litho-types of varying resistivity parameter, making MT/AMT studies to be useful for the detection of near surface and, or deep regional conducting anomalies (Zhang et al., 1995). Recently, Singh et al. (2018) carried AMT sounding over the same area in frequency range of 10 kHz–10 Hz. The direction along which the physical properties vary minimally is termed as strike. The strike analysis over the regional AMT profile in the frequency range of 1 kHz–10 Hz shows that it varies both with frequency as well as site indicating towards complex structure (Singh et al., 2018). However, they performed 2-D AMT inversion to obtain an approximate conductivity image.

2-D interpretation of 3-D data is common practice in MT studies. Regional scale surveys are often restricted to a profile or widely separated profiles due to high cost and inaccessibility. But there are many cases where data have been acquired over highly dense 2-D grids for geothermal studies (Park and Torres-Verdin, 1988; Takasugi et al., 1992; Park and MacKie, 2000) and mining-scale problems (Zhang et al., 1998; Tournerie et al., 2000). Limitations and problems of 2-D

interpretation of 3-D data have been studied over last few decades (Jones and Vozoff, 1978; Kaufman and Keller, 1981; Ting and Hohmann, 1981; Hermance, 1982; Park et al., 1983; Jones, 1983; Berdichevsky and Zhdanov, 1984; Wannamaker et al., 1984; Park, 1985; Wannamaker et al., 1991, Berdichevsky et al., 1998; Berdichevsky, 1999; Wannamaker, 1999). A major issue of approximating 3-D electrical structures that lie off-profile using 2-D inversion methods is the possible mischaracterization of 3-D effects as unwanted features in 2D models. The factor that validates 2-D interpretation of 3-D structures depends on the relationship between the frequency of interest, size of the anomalous structure and distance of the anomalous structure from the 2-D profile (Garcia et al., 1999).

The presence of off-profile structures affects most data sets to at least some degree (Brasse et al., 2002). Significant, off-profile conductivity anomalies that diminish the assumption of along strike invariability of structure are best accommodated by undertaking 3-D inversion that don't require an established strike direction for resulting models.

Patro and Egbert (2011) mentioned that the possibility to find a unique strike, which can be optimal for the entire frequency range and for all the sites and possible impact of off-profile structure, should always be considered. Siripunvaraporn et al. (2005) showed that the inversion of even single profile MT data with the 3-D algorithm results in more realistic images beneath the profile and, if the full tensor is fit, may even provide limited resolution of off-profile structures. This tempted us to perform 3-D AMT inversion for the regional AMT profile over Dhanjori Basin which includes DhV and quartz-pebble-conglomerate of Dhanjori (QPCD) (Fig. 1a) and showed varied strike direction (Singh et al., 2018). 3-D AMT inversion has been attempted using Modular system for Electromagnetic Inversion (ModEM) (Egbert and Kelbert, 2012; Kelbert et al., 2014) for the entire frequency range of 10 kHz–10 Hz. Inversion was executed to identify and map the shallow

Table 1
Generalized stratigraphy of Singhbhum (after Saha, 1988; Upadhyay et al., 2014) and North Singhbhum Crustal Province.

Age (Ga)	Singhbhum Nucleus	Singhbhum-Dhalbhum Mobile Belt	Chotanagpur Belts
0.9–1.6	Newer dolerite		Syn-to-late-and post Tectonic, granites/gneisses
1.5	Kolhan Group		
1.6	Gabbro/anorthosite	Chakradharpur Granite; gabbro/anorthosite	Gabbro/anorthosite
	Ultramafic intrusion	Chandil Formation	
Unconformity			
	Dhanjori Group (Study Area)	Dalma lavas	
Unconformity			
	Singhbhum Group(Chaibasa formation)	Singhbhum Group	
Unconformity			
2.9	Singhbhum Granite; Iron Ore Group		Orthogneisses
Unconformity			
3.45	Older Metamorphic Group Gneisses		
3.6	Older Metamorphic Group supracrustal rocks		
	Basement?	Basement?	Basement?

subsurface electrical conductivity distributions and possible mineral potential associated with Dhanjori basin. Since geophysics is being used to describe geology, we try to explain the links between physical properties and geological features. With the available data of susceptibility, density and chargeability of core samples be deliberated on regional metamorphism and serpentenization and tried to identify and quantify the presence of oxides and sulphides. Further, we have also investigated the petrophysical properties influencing mineralization. The study integrates the audio magnetotelluirc data, petrophysics and geology in understanding the mineralization and optimizing the drilling locations.

2. Regional geology

Dhanjori basin is situated in the northeastern part of the Singhbhum-Orissa Craton i.e., Archean Cratonic Core Region and fringes at the north and northeastern part by Singhbhum Shear Zone (SSZ). SSZ separates the basin from the supracrustals of North Singhbhum Mobile Belt (NSMB) (Table 1, Fig. 1a) (Misra and Johnson, 2005). The basin has a broad triangular outline and inward dips in its western and southern part, which indicates a central synclinal structure (Fig. 1a). At its northern and northwestern part, the basin shows intense transgression across the SSZ and the formations are turned into asymmetrical westwards overturned folds (Mahadevan, 2002). Dhanjori Group of rocks overlies unconformably on the Singhbhum granite basement and commences with a basal polymictic conglomerate, which is further overlain by a thick sequence of volcano-sedimentary sequence. Although the conglomerates are confined all along the northern margin of the granitic basement at some places these are more prominent with its thickness at around 100 m.

The 2.1-Ga-old Dhanjori Formation (Roy et al., 2002) is composed of siliciclastic sedimentary rocks interlayered with mafic to ultramafic and rare acidic volcanic and volcaniclastic rocks. The rocks are deformed and are of low-grade green schist metamorphic facies (Dunn and Dey, 1942; Iyenger and Alwar, 1965; Sarkar and Saha, 1962, 1977; Sarkar, 1984; Gupta et al., 1985; Basu, 1985; Singh, 1998; Singh and

Nim, 1998). Interbedded volcanics and volcaniclastics in different stratigraphic level within the upper member, however, indicate episodic volcanic eruption during sedimentation (Mazumder and Sarkar, 2004).

2.1. Geology of the study area

Dhanjori Group of rocks has been further subdivided into two formations. The lower formation is composed of a phyllite with minor mafic-ultramafic intrusions, whereas the upper formation consists of arkose, conglomerate and phyllite with its gradual transition into a predominantly volcanic association. Mafic volcanic rocks of Neoarchean to Paleoproterozoic age with Neoarchean quartz-pebble-conglomerates at the base are the characteristics of Dhanjori basin (Acharyya et al., 2010).

The Lower Dhanjori Formation is dominated by sediments and is subdivided into two units (Gupta et al., 1985). The upper unit consisting of quartzite–polymictic conglomerate interlayered with phyllites and tuffs is termed as Lower Dhanjori Formation. The basal part of the sequence, which consists of phyllites, Au–U-pyrite bearing quartz-pebble-conglomerate (QPC), acid volcanic rocks, acid (rhyolitic) and basic tuffs, and mafic–ultramafic intrusive rocks is identified as an infra-Dhanjori unit, which is termed Phuljhari Formation. The Mayurbhanj Granite is intrusive into the QPC bearing Phuljhari Formation and it is non-conformably overlain by the Dhanjori Group. The Upper Dhanjori Formation is a mafic volcanic rock dominated unit. The generalized stratigraphy sequence of Dhanjori Group (Gupta et al., 1985) is given in Table 2.

Significant concentration of gold values has been obtained from the Dhanjori metavolcano-sedimentary sequence. Ultramafic rocks, non-vesicular metabasalt, and felsic volcanics consists of around 0.250 ppm, 0.470 ppm and 4 ppm of gold respectively, whereas quartzite, phyllite and QPC were reported for 0.900 ppm, 0.080 ppm and 2.4 ppm respectively (Ghose, 1996) reported presence of gold in the basal part of Dhanjori basin, which ranges from < 0.025 ppm to 4 ppm. The geochemical analysis of systematic channel samples indicated anomalous

Table 2
Generalized Stratigraphic sequence of Dhanjori Group (after Gupta et al., 1985).

Dhanjori Group	Upper Dhanjori Formation	Tholeiitic basalt (locally pillowed), Mafic–ultramafic tuffs and intrusives, tuffaceous sediments
	Lower Dhanjori Formation	Quartzite (locally arkosic) with discontinuous polymictic conglomerate, interlayered with tuffs
	Non-conformity	
	Mayurbhanj Granite	
	Phuljhari Formation	Ultramafic–mafic intrusives, Purple and greenish phyllite, gritty and pebbly shale, acid–mafic tuff–tuffite, volcanics, Quartzite with lenses of QPC
	Non-conformity	
	Singhbhum Granite	

gold value in ~58% of the QPC of Dhanjori (QPCD) samples in the range of 0.5 ppm–7 ppm (Haque and Dutta, 1996). Singh et al. (2018) analysed the samples collected from the QPCD using Inductively Coupled Plasma Atomic Emission Spectroscopy (ICP-AES) and indicated an average value of gold as 5 ppm.

The gold occurrences within the Dhanjori Basin are mainly confined to mafic/ultramafic meta-volcanics within the quartz ± carbonate vein of Dhanjori group (Haque and Dutta, 1996: Mazumder and Sarkar 2004, Chakravarti et al., 2017). Within this gold mineralization is associated with other sulphides i.e., chalcopyrite, sphalerite, galena, arsenopyrite, pyrite and antimonite. Within QPC the gold occurs in detrital form as placers where the host rocks are pebble conglomerates and quartzites. The other associated ore minerals are magnetite, pyrite, ilmenite, uranium, and monazite. Singh et al. (2018) reported average concentration of silver, copper, uranium, magnetite, lead and zinc as trace, 110 ppm, 50 ppm, 1.5 ppm, 6.5 ppm and 55 ppm respectively for the rock samples collected over QPCD.

Verma et al. (1966) reported terrestrial heat flow and geothermal gradient of ~61 mW/m^2 and ~20 °C/km respectively in Dhanjori Volcanics. The existence of the Dhanjori basalts including komatiites and komatiitic basalts within upper members of DhV implies subsequent upwelling of mantle plume and decompression melting following crustal extension (Mazumder and Sarkar 2004). Thus, crustal extension and extensive crustal thinning beneath the Dhanjori Volcanics along with high geothermal gradient and rifted margin gives rise to metallogeny in form of rifted phase greenstone belts with gold enriched sulphide mineralization.

3. MT/AMT method

The MT/AMT method employs measurements of natural-source electromagnetic (EM) fields that induce currents in an electrically conductive Earth. These currents give rise to secondary EM fields, and MT/AMT entails measuring time series of electrical and magnetic fields at the Earth's surface that are a superposition of natural- and secondary-source fields (Tikhonov, 1950; Cagniard, 1953). The measured components of two electrical and three magnetic fields are (E_x, E_y) and (H_x, H_y and H_z) respectively. The natural EM source fields are generated by large-scale ionospheric current systems that are relatively far away from the Earth's surface (Viljanen, 2012). Thus, the source is treated as uniform, plane-polarised EM waves impinging on the Earth at near-vertical incidence (Simpson and Bahr, 2005). The measured electric and magnetic field components helps in determining the rank 2 impedance tensor

$$Z_{ij}(\omega) = \frac{E_i}{H_j}$$

(1)

where $i, j = x, y$ and ω is the angular frequency. Impedance is a complex quantity, which has both amplitude and phase. The amplitude of impedance tensor is termed as apparent resistivity

$$\rho_{a_{ij}} = 0.2T\ |Z_{ij}|^2$$

(2)

where T is the time period.
and phase can be determined as,

$$\phi_{ij} = \arg\left(\frac{E_i}{H_j}\right)$$

(3)

The vertical magnetic field component is related to the horizontal magnetic field components (Vozoff, 1972). EM fields which are utilized for MT/AMT studies are naturally induced in the Earth and have periods ranging from ~10^{-4} s to ~10^5 s (Simpson and Bahr, 2005). The EM skin depth or penetration depth is the depth at which the EM field attenuates to (1/e) of their amplitude at the surface of the Earth. EM skin depth can be determined as,

$$\delta \cong 500 \times \left\{ \frac{resistivity}{frequency} \right\}^{1/2}$$

(4)

Thus, it depends on the bulk resistivity of the overlying material and the frequency used. In the geological terrains with high resistivity, MT signals have larger penetration depths. The broad range of the depth that is detectable using this method gives it an advantage over other technique (Simpson and Bahr, 2005). This method is highly sensitive to variation in distribution of minerals (including sulphides, etc.) and fluids within the rock matrix inside the Earth as these factors can cause bulk electrical conductivity to vary by several orders of magnitude (Chave and Jones, 2012; Simpson and Bahr, 2005).

The present analysis is based on 18 AMT sites with the frequency range of 10 kHz–10 Hz. Singh et al. (2018) acquired data for 14 sites 01, 02 03, 04, 05, 06, 06′, 07, 07′, 08, 08′ 09, 09′ and 10 whereas 4 new sites namely 01′, 03′, 04′ and 05′ has been acquired additionally for the present study. Both the data sets have been acquired in the frequency range of 10 kHz–10 Hz. Although Singh et al. (2018) used data sets from 1 kHz to 10 Hz.

Sites 01, 01′, 02, 03 are over DhV, 03′, 04 , 04′ over QPCD, 05′, 05, 06 , 06′ and 07 are over MG, 07′, 08 and 08′ over PGAU and 09, 09′ and 10 are over IOG (Fig. 1b). On an average, the site separation is ~1.0 km. The time series for all five components were collected for six hours at each site using MTU-5A equipment from Phoenix Geophysics Ltd. Pb-PbCl2 electrodes were used for acquiring the electric field while the magnetic fields were measured using induction coils. The length of the electrical dipole was ~100 m.

3.1. AMT data analysis

Scatter in the data indicates that the data is biased, whereas error bars indicate the precision of the estimates. Scatter data could have small error bars (Gamble et al., 1979a,b). Thus, a good quality of the data is assessed by both low scatter and small error bars. In general, the robust processing of the MT data is performed. The robust estimates are insensitive to outliers and the weights are inversely proportional to the residual (Huber, 1981). In view of this, Shalivahan et al. (2006) proposed extra hybrid approach and processed the MT time series. The extra hybrid combines all the three possible weights i.e., coherence weighted estimate (CWE), rho variance and robust estimate. CWE down weights the low coherency between E_x and H_y and improves the signal to noise ratio (Stodt, 1983). Whereas, rho-variance down weights the high coherency between H_x and H_y and improves the signal to noise ratio (Stodt, 1983). Thus, the extra hybrid approach helps in reducing the influence of both the outliers in the electric field and the leverage points (i.e., the noise on magnetic field). The processing resulted in precise estimation of the data even in AMT dead band. The AMT data is considered for three decades including the dead band 1 kHz–2 kHz. The data in the frequency decade 10 kHz–1 kHz is less noisy as compared to the data in the other decades. Thus, extra hybrid approach of Shalivahan et al. (2006) resulted in bias error in AMT dead band and these were not considered for further analysis (Fig. 2). Complex-valued impedances for four stations, plotted as apparent resistivity and phases for the off-diagonal elements of the 2 by 2 impedance tensor, along the direction of acquisition, are given in Fig. 2.

All the stations were acquired along the north-south and east-west directions for electric and magnetic fields. For the site 03, which is close to the borehole, B1 (Figs. 1a, b), it is observed that the apparent resistivities of the xy and yx component are close to 50 Ωm for shorter periods which increases with increasing period. The phase data shows the decrease in phase with decreasing frequency. The apparent resistivity data for site 04 for shorter periods starts around 1000 Ωm and it increases to values greater than 10,000 Ωm. The high apparent resistivity for shorter periods hint towards presence of resistive terrain at a shallow depth. For site 05 it is observed that the apparent resistivity
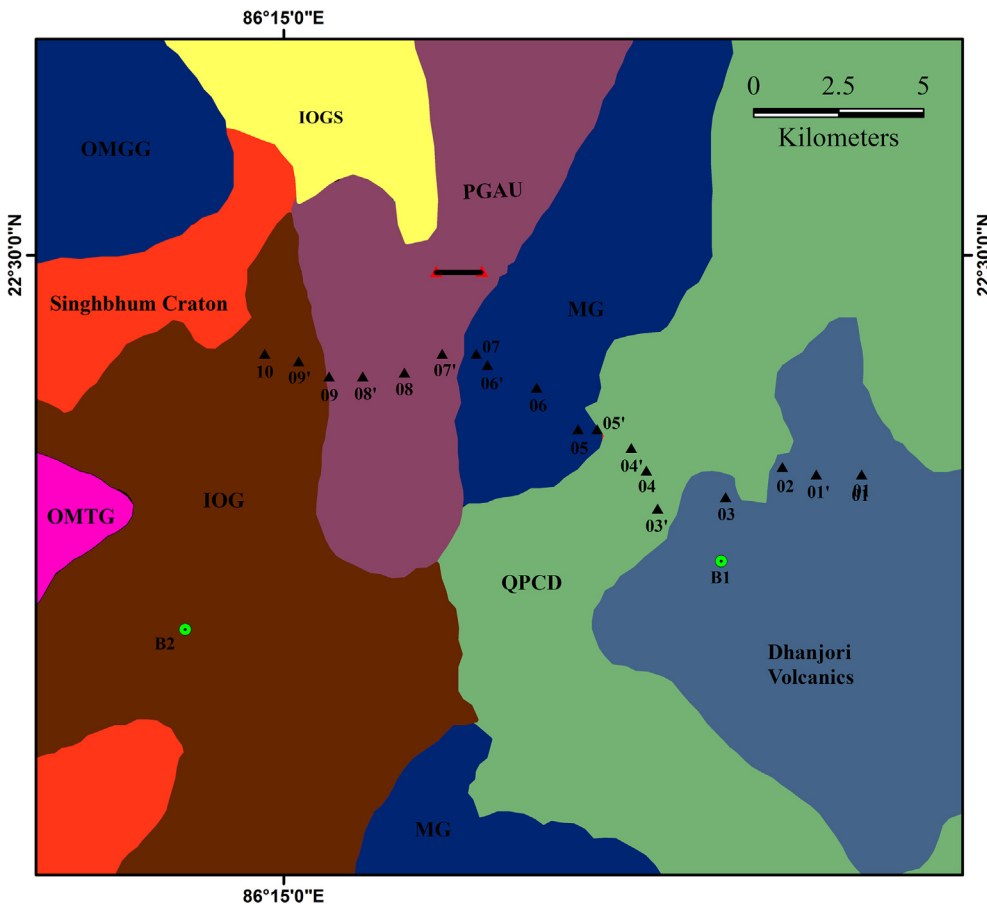
Fig. 1b. Detailed geological map showing the distribution of AMT sites (black triangle). Green filled circle with a dot represent the borehole (B1; Das et al., 2008) and (B2; Kundarkocha Gold Mine). Red triangle represent the western and eastern ends of profile along which Gupta et al., 2018), performed Electrical Resistivity Tomography. (For interpretation of the references to colour in this figure legend, the reader is referred to the web version of this article.)

increases from 10 Ωm to values greater than 1000 Ωm. The phase data first decreases and subsequently increases.

The data for 09, which is close to borehole B2, shows that the apparent resistivity increases from ~100 Ωm to more than 1000 Ωm. However, the higher and intermediate frequencies show different trend for different sites but at the lowest frequency for all the sites phase shows an increasing trend. This probably indicates towards a thin conducting feature at deeper depths.

3.2. Dimensionality and strike analysis

The dimensionality analysis has been performed using Swift skew, Phase sensitive skew (PSS) , WAL invariants, and Phase tensor for entire frequency range 10 kHz–10 Hz rather than 1 kHz to 10 Hz as performed by Singh et al. (2018) for their sites. The values of Swift skew are 0.2 for 1-D and 2-D structures (Swift, 1967). Higher skews indicate 3-D structure or higher levels of noise. The PSS (Bahr, 1991), is relatively insensitive to galvanic distortion effects, and gives a better estimate of the dimensionality than the Swift skew. For, PSS greater than 0.3, the data should be considered as 3-D (Bahr, 1991).

Fig. 3 shows value of Swift skew and PSS which indicates towards the presence of 3-D structure. Fig. 4 (left panel) shows that the phase sensitive strike varies for DhV and QPCD. Whereas, for Mayurbhanj granite, PGAU and IOG (Fig. 4, right panel) two well resolved strike directions one N45ºE and other N 45ºW is seen. Similar to Fig. 3, Fig. 4 also indicates towards complex structure.

The dimensionality analysis has also been attempted by using the revised version of the WALDIM code (Marti et al., 2009) which is based on the invariant rotation parameter of the impedance tensor (Weaver et al., 2000). The results from the WALDIM code for each AMT site and for the entire frequency range have been plotted in Fig. 5a and using the criteria established by Weaver et al. (2000), the dimensionality analysis

of the data has been performed.

As is evident from the Fig. 5a that for almost all the sites and for large number of periods the dataset shows the 3D feature.

Caldwell et al. (2004) and Bibby et al. (2005) introduced the methods of phase tensor (PT) for analysing the MT/AMT data, which are very useful especially when the data are galvanically distorted. The geometry of phase tensor is an indicator of directionality and dimensionality of the dataset. The most important characteristic of this technique is that it makes no assumptions about the dimensionality of the regional response tensor and is unaffected by the presence of electric field galvanic distortion. The phase tensor are graphically presented as an ellipse whose major and minor axes represents the principal axes of the tensor (Caldwell et al., 2004) where the phase tensor principal axes reflect lateral variations in the underlying regional conductivity structure. Using four phase tensor parameters namely maximum (Φ_{max}) and minimum (Φ_{min}) phase values, the skew angle (β) and the non-variant angle (α), a possible comment on the dimensionality can be made. Further, Bibby et al. (2005) introduced a dimensionless parameter ellipticity (λ) which is combination of first two. For 1D case, both β and λ are zero. For 2D (and 3D/2D), β is zero while λ is non-zero. For 3D, both β and λ are non-zero (Bibby et al., 2005). For 1D structure, the ellipse reduces to circle and in 3D structures, the orientation of major axis of ellipse varies with period.

The skew angle (β) changes value from $-16°$ to $16°$ (Fig. 5b) and also the shape of the ellipses are rarely circular and more over the orientation of the ellipses i.e., the direction of the major axis which determines the strike is not consistent which also hints towards the complex structure in the data. Further, the non-zero ellipticity (λ) (Fig. 5c) also indicates the 3D structure.

Caldwell et al. (2004) stated that the effect of conductivity structure shrinks the ellipses to a line. This is evident for short periods for both site 03 and 09 (Fig. 5b and c). Thus, the ellipses collapsing to line may
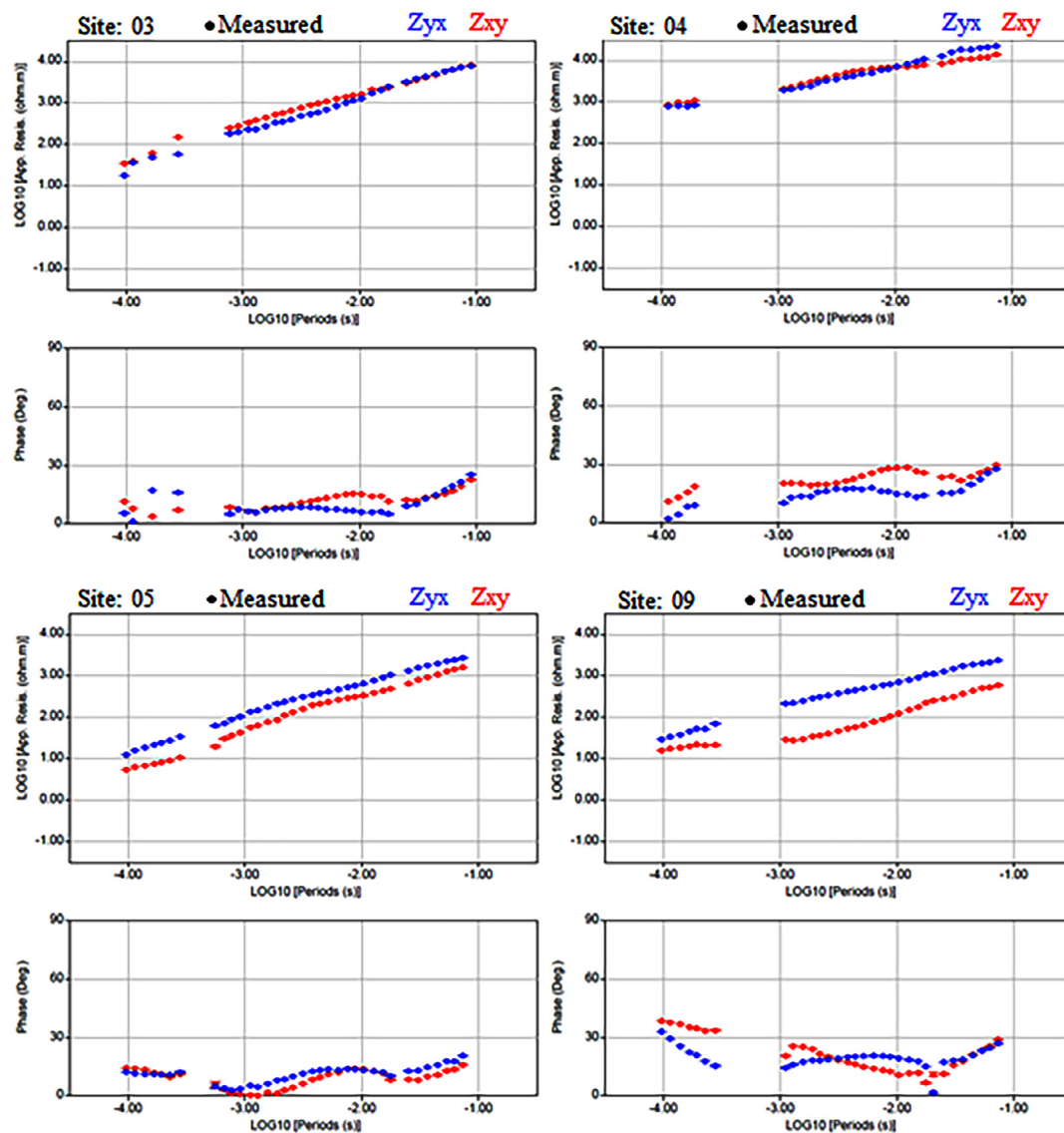
Fig. 2. Observed data for some of the representative sites DH 03, DH 04, DH 05, and DH 09.

be indication of conductivity anomalies below the site 03 and 09. Thus, both WALDIM and PT analysis approaches confirms the presence of 3-D structures for all the sites, consistent with swift and Bahr skews.

4. 3-D Audio Magnetotelluric studies

3-D inversion of AMT data has numerous advantage over 2-D which makes it very useful. The limitation and shortcoming involved with 2-D inversions of a 3-D data have been demonstrated with synthetic (Ledo, 2005) as well as field (Newman et al., 2003; Simpson and Bahr, 2005)
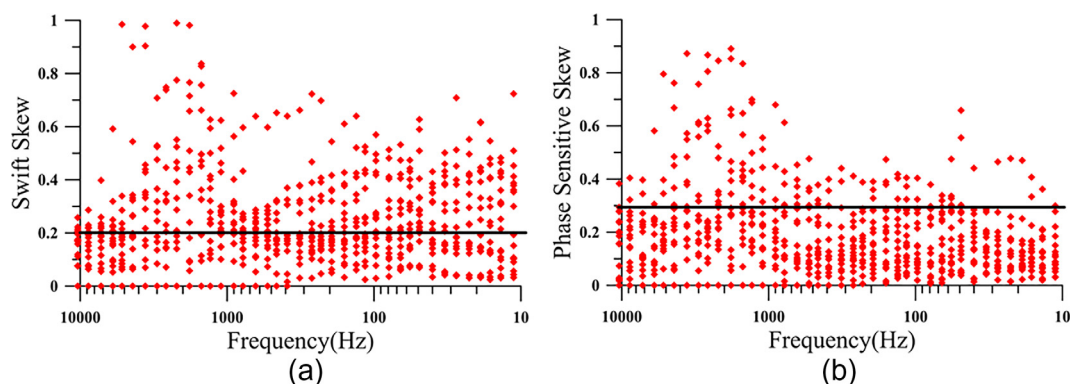
Fig. 3. Swift skew (left) and Phase Sensitive Skew (right) for all sites for 10 kHz- 10 Hz.
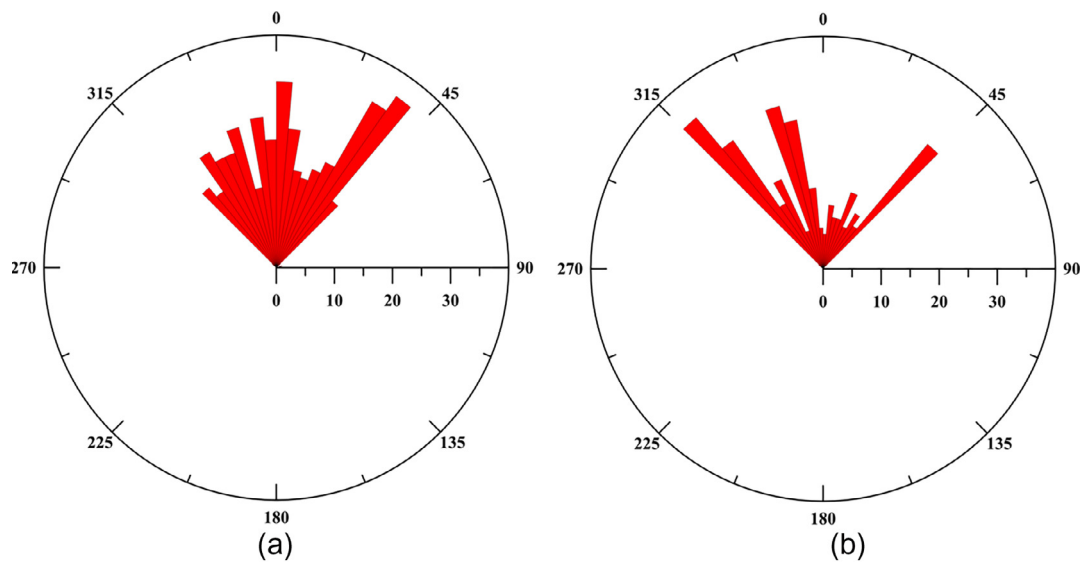
Fig. 4. Rose diagrams showing phase sensitive strike direction: (left) Dhanjori Volcanics and Quartzite-Pebble-Conglomerate of Dhanjori Group of rocks, (right) Mayurbhanj granite, Proterozoic gabbro-anorthosite (PGAU); and Iron Ore group of rocks.

study. Inverting MT profile data with 3-D inversion helps in avoiding contamination by out of plane/off-profile structures (Siripunvaraporn et al., 2005).

For 2-D inversion, the data needs to be projected on to the same profile, which also affects the final model whereas with 3-D inversion, data from sites scattered in space can also be used without any projection. This prevents errors in estimation of size, shape and location of the structures (Siripunvaraporn, 2012).

Among the other advantages of 3-D inversion is that it can fit the inductive effects due to localized near-surface structures both directly beneath and outside the station. 3-D inversion also finds its utility in obtaining the galvanic distortion or the static shift (Newman et al., 2003; Sasaki, 2004; Sasaki and Meju, 2006; Meqbel et al., 2014) by discretizing the model near the surface very fine. It also recovers the L-shape structure that produces phases more than 90° (Ichihara et al.,

2010) unlike the 2-D inversion.

5. Setting of inversion parameters

3-D inversion of full impedance component has been attempted for all the sites for full impedance component in the frequency range $10\,kHz - 10\,Hz$. 3-D inversions of MT/AMT data is a non-linear problem, which makes it an iterative minimization process. The choice of initial model can influence the result (Hersir et al., 2013). 3-D inversion of full impedance component can be influenced by the choice of initial half-space resistivity and error floors. 3-D inversion of off-diagonal component was performed to obtain the optimum value of initial uniform half-space resistivity and error floor of off-diagonal component. We discretized our model with various grid size as 500 m, 400 m and 250 m in X and Y directions and keeping the other parameters fixed.
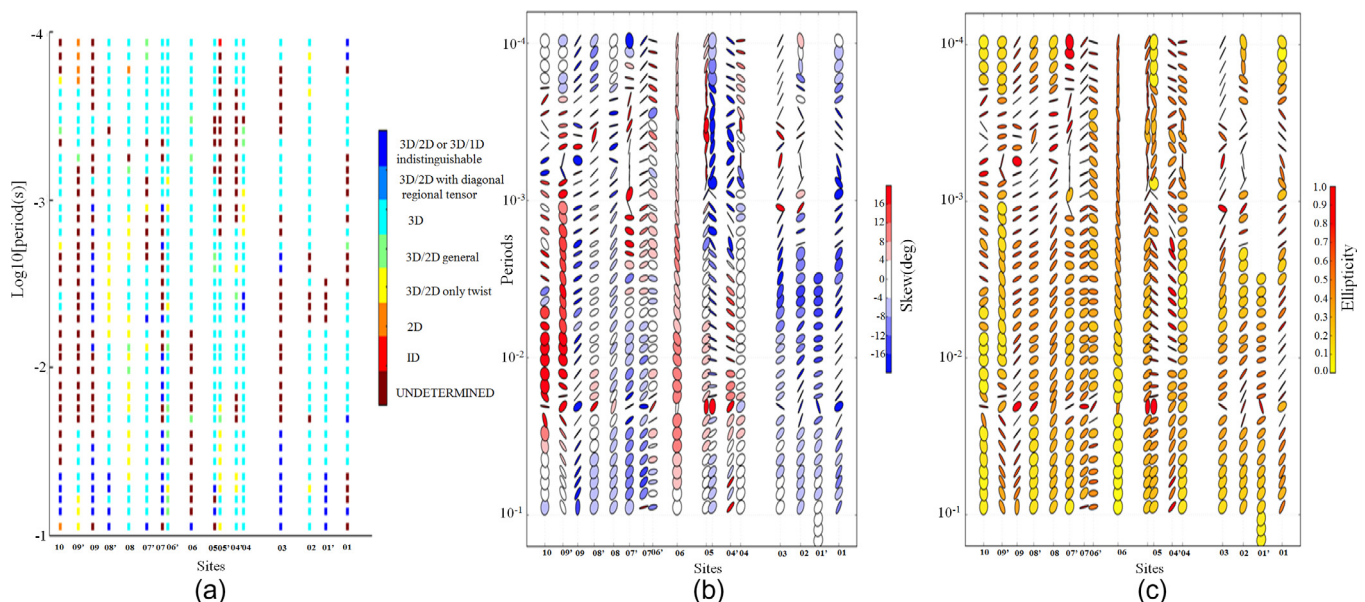

Fig. 5. Dimensionality analysis results using the (a) WALDIM, (b) Phase tensor skew angle (β) and (c) Phase tensor ellipticity (λ) pseudo section plots for the periods, 0.0001 s-0.1 s. for AMT site layout, Skew angle significantly deviates from zero (red and blue colouring) indicating presence of 3-D feature in the data. Skew angle (β) has been plotted with threshold|β| = ± 4. Dimensionless parameter (λ) ≠ 0 for most of the site and for all the frequency. λ has been plotted with threshold of 0.1. (For interpretation of the references to colour in this figure legend, the reader is referred to the web version of this article.)
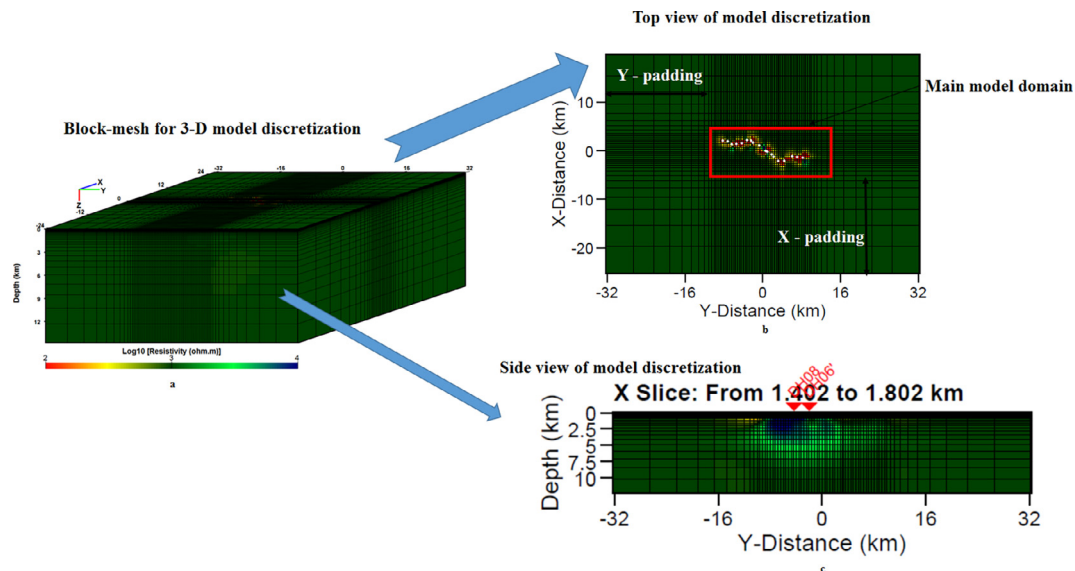
Fig. 6. (a) 3-D model block mesh discretization with 15 X 50 X 30 cells in ×, y and z directions. (b) Top view of 3D model mesh in × and y directions, shown red rectangle is the main modeling domain, 10 padding cells were included to avoid the edge effect in the main model domain. (c) Side view of model mesh in y and z directions. Vertical mesh increases with a factor of 1.2 in z direction up to depth of ~11.8 km. (For interpretation of the references to colour in this figure legend, the reader is referred to the web version of this article.)

These provided us the RMS of 4.72, 3.52 and 3.6 respectively. Keeping the grid size of 400 m gives, minimal RMS of 3.52 and it also provide at least two cells between adjacent stations. In addition, grid size of 400 m provides model features consistent with a priori geological information. Thus, we used 400 m grid cell for all subsequent inversion runs. In Z direction, average skin depth (~15 m) for all MT stations for highest frequency was tested for first layer thickness initially. Finally, we used smaller first layer thickness (~5 m) to include near surface heterogeneities. Fine mesh discretization may help us in the modeling of static shift present in the data as well improvement in data fits. The shallow surface heterogeneities in cases distort the longer periods of MT/AMT data, which causes severe static shift to the model results. To tackle static shift fine mesh model discretization was applied in the vertical direction at shallow depths (Meqbel et al., 2014).

To carry out 3-D inversion both for off-diagonal and full impedance, the model domain was finally discretized into 15, 50, 30 cells in x, y and z directions respectively with the dimension of 0.4 km each along y and y direction respectively (Fig. 6a and b). The thickness of first cell along z directions is 5 m, which increases by a factor of 1.2 and the maximum size of the model in the z direction is 11.8 km (Fig. 6c). Ten padding cells with an increment factor of 1.5 are also included both in X and Y directions to avoid the edge effect in the main model domain (Fig. 6b). The main model domain consisting of AMT sites must be far enough from the edges of the model to avoid the edge effect. The horizontal adjustment length is the lateral distance to which an MT transfer function of a given period is sensitive which is generally two to three times of the skin depth (Simpson and Bahr, 2005). This can help in deciding the model dimension which is not affected by the edge effect. The minimum frequency of 10 Hz with 1000 ohm-m half space model results in skin depth of ~5 km, thus horizontal adjustment length is ~10–15 km. The length of 10 padding cells in the model is ~22 km in both X and Y direction respectively. Thus, providing 10 padding cells in models mostly avoid the edge effect at the model boundaries.

To check the optimum values of initial half-space resistivity, inversions using off-diagonal components data have been carried out using various initial half-space uniform resistivity of 100 Ωm, 500 Ωm, 1000 Ωm and 1500 Ωm respectively (Fig. 7) with the error floor of 5% of $|\sqrt{Z_{xy}Z_{yx}}\|\sqrt{Z_{xy} \times Z_{yx}}|$ resulting in RMS of 3.12, 2.96, 2.86 and 2.95 respectively. Inversions were started with a large value of lambda, a

trade-off parameter in a penalty function. Penalty function comprises of data misfit and model roughness. Initially lambda takes care of model roughness. As inversion progress, the lambda is reduced by a factor of 10. Throughout this process, a relatively small minimum threshold (~0.001) for a fixed lambda is maintained for iterative step-wise for reduction of data misfit (Kelbert et al., 2014).

Comparative conductive feature develops below sites 06 to 08 (Fig. 7a, b). This conducting feature can be seen underlying a very resistive feature but the apparent resistivity data does not reflect this contrast. The phase data in the last band shows that resistivity decreases at larger depths (Fig. 2) which is observed in Fig. 7c unlike Fig. 7d. The minimum RMS is obtained for Fig. 7c. Therefore, on the basis of model features and RMS we have considered 1000 Ωm as the final value of initial half-space uniform resistivity for 3-D inversion of full impedance. The high value of initial homogenous half-space resistivity is also supported by the fact that when Φ_{min} was plotted for all the sites with varying periods it showed the value < 45° (Figure not shown) which itself signifies that the study area is dominantly resistive in nature.

To ascertain the optimum value for error floor on all the component of impedances for carrying out the 3-D inversion, number of inversion runs were performed with following combination of error floors (i) error floor of 10% and 5% to the diagonal components and off-diagonal components respectively resulted in RMS of 3.32 which is quite high, (ii) error floor of 20% and 5% to the diagonal components and off-diagonal components respectively resulted in RMS of 2.64, (iii) error floor of 20% and 10% to the diagonal component and off-diagonal components respectively resulted in RMS of 1.83, and (iv) error floor of 10% for diagonal component and off-diagonal components respectively resulted in RMS of 2.3. Assigning higher error floor results in down weighting the particular component and hence, a compromise was made between higher error floor and lower RMS. Therefore, the error floor of 10% for each components of impedance tensor was chosen as the final value.

Fig. 8 shows the model obtained from the 3-D inversion of full impedance component using initial uniform half space resistivity of 1000 Ωm and error floor of 10% for both diagonal component off-diagonal components.

Fig. 8a shows the model extended to 4 km depth with identified geological boundaries and mineralized zone and Fig. 8b shows the same
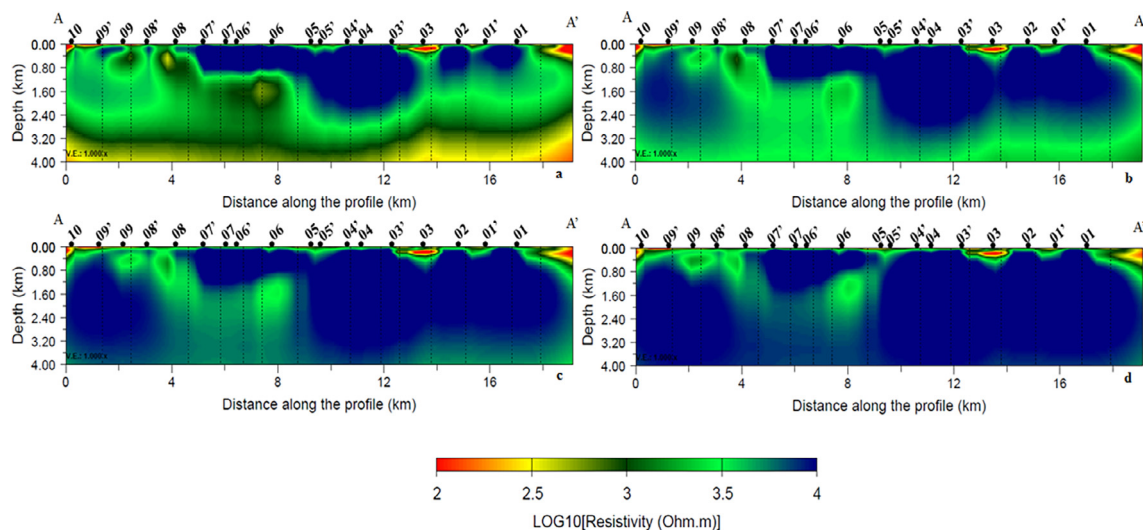
Fig. 7. Off-diagonal inversions results with fixed error floor of 5% of product of off-diagonal components with four different initial half-space uniform resistivity a) 100 ohm-m; b) 500 ohm-m; c) 1000 ohm-m; d) 1500 ohm-m with RMS of 3.12, 2.96, 2.86 and 2.95 respectively.
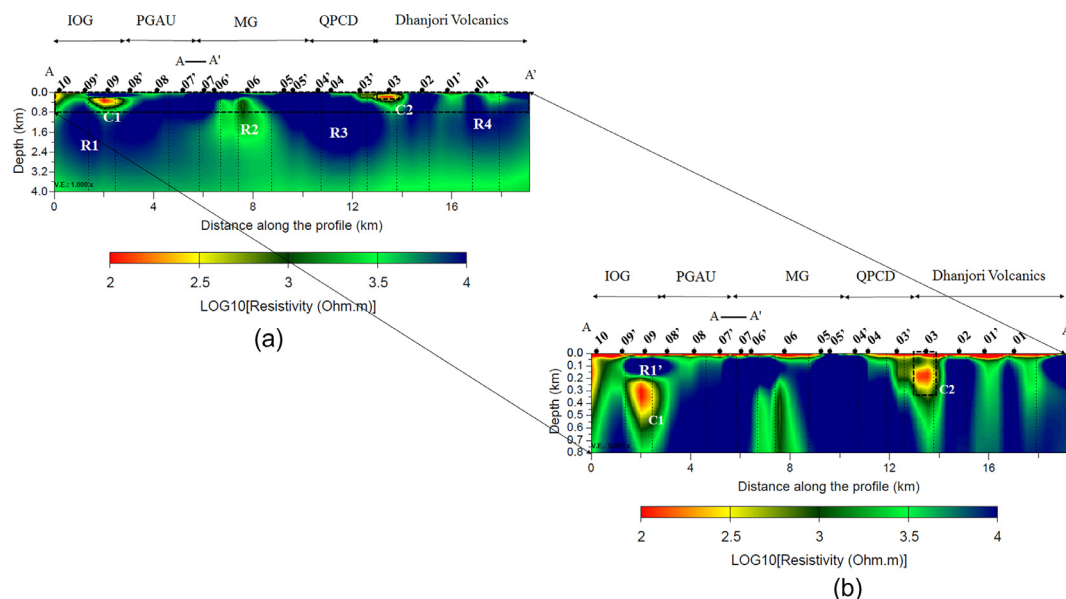

Fig. 8. Cross-section for the model after 3-D Inversion of Full Impedance component with RMS of 2.3. (a) Cross-section with depth of 4 km. The four resistive zones viz., R1, R2, R3 and R4 and two conducting zone C1 and C2 are zone of importance and are discussed in the text. The discontinuous rectangle at shallow depth in the model (Fig. 8a) which is magnified as Fig. 8b. (b) Cross- section representing the model to a depth of 800 m.

to a depth of 800 m. The figure shows the location of drill hole (Das et al., 2008) which is close to AMT site 03 in Dhanjori Volcanics indicated by the discontinuous rectangle (Figs. 8a, 7b).

Conducting zones C1 and C2 (Fig. 8b) are similar to Fig. 8a. Resistive zone R1′ that was not clearly appearing in Fig. 8a clearly appears here.

Iron Ore Group (IOG) is believed to be late Archean age and occurs along the western margin of Singhbhum Granite. These were deformed during Iron Ore Orogeny and were disposed in a horseshoe shaped synclinal structure. These occur either as linear narrow intra-cratonic belts or as mode extensive peripheral bodies. It consist of banded iron formation (BIF) and metasedimentary and metavolcanics rocks. Saha (1994) stated that the northerly plunging asymmetric synclinorium IOG rocks include BIF and low-grade meta-sediments including BIF, phyllites, tuffaceous shales, quartz arenite, argillite, ferruginous quartzite, dolomite, mafic and ultramafic volcanic rocks. It occurs in the western, eastern and southern flanks of Singhbhum Granite. Banerjee (1982)

explained these BIF to be interbanded with lavas and pyroclastics and even basic volcanics interbedded with rhyodacite and trachytic volcaniclastics. IOG are composed of iron bearing sediments (Verma et al., 1984), alternate layers of iron rich materials and silica (Bandopadhyay and Sengupta, 2004). These might have resulted in high resistivity of R1 (Fig. 8a) (Telford et al., 1990) coincident with N-S trending high gravity anomaly over IOG (not shown) (Verma et al., 1984). The gravity over IOG is attributed to high-grade gneisses, schists and volcanics. It hosts high-grade iron ore deposits in eastern India. Banerji (1977) stated that within the sequence of predominantly volcanogenic metasediments of IOG, Precambrian banded iron formations and manganese ores occurs around a central granitic platform. It is similar to the conducting zone (C1) which is sandwiched between overlying and underlying two resistive features and appears as interbanded sequence (Banerji, 1977). The presence of the conducting feature above the granitic platform may be formed due to the volcanic rocks accumulated by the thrust zones surrounding the Singhbhum granitic platform. This
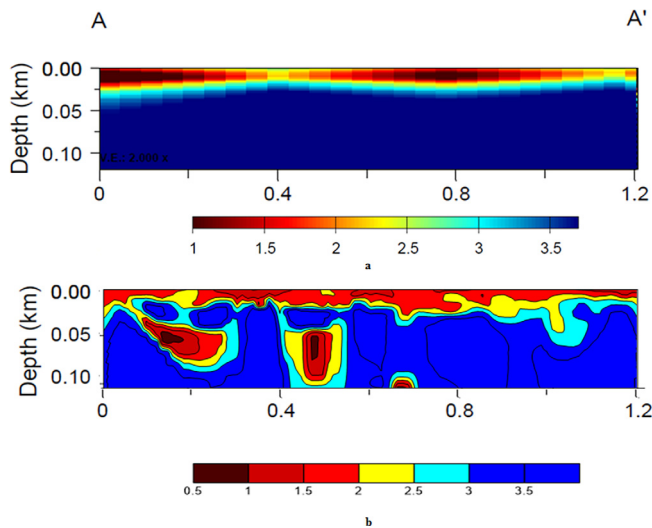
Fig. 9. Comparison of AMT cross section (top) close to the profile over which ERT survey was done by Gupta et al. (2018) and Inverted ERT model section (bottom) with dipole-dipole arrangement.

explanation is strongly validated by the fact that the northern thrust zone appeared after the emplacement of Singhbhum granite, along which the eruption of basic and ultra-basic rocks and pyroclastic material occurred (Banerji, 1969).

Dunn and Dey (1942) grouped PGAU under basic rock and are associated with the Iron Ore "Stage". There is no clear difference observed between IOG and PGAU (Fig. 8a). The resistive feature R1 continues its extension in the eastern direction of the profile and it shallows as one move towards PGAU.

This may be due to the fact that PGAU are intrusive into the IOG (Chakraborty et al., 1981) and the mafic-ultramafic lavas and the gabbro-anorthosite intrusions are considered as co-magmatic bodies belonging respectively to volcanic and plutonic phases of the same

protolith sources.

Saha (1975) explained Mayurbhanj Granite (MG) as batholithic body with irregular shape forming a roughly crescentic area. It is made up of following units:a) fine-grained, near homophanous, granophyric biotite-hornblende-alkali feldspar granite; b) coarse grained, near homophanous to well-foliated ferrohastingsite-biotite granite locally with ferrohedenbergite and is intrusive into the granophyric unit; c) biotite aplogranite injected into above unit. This makes the entire domain resistive. Further, a resistive feature R2 extending to a depth of 1.5 km (Fig. 8a) occurs at the western margin of MG. This resistive feature may be associated to the high-density basic/ultrabasic rocks that do not allow passage for electrolytic conduction which may lead to higher resistivity of R2. The resistive features R1 and R3 are connected and are underlain by another resistive feature R2. MG intrudes the quartz-pebble conglomerate (QPC) and volcaniclastics bearing unit at the base of the Dhanjori basin. This is similar to resistive feature R3 (Fig. 8a) where the resistive feature lies below conductive feature lying at a shallow depth within QPCD. The Dhanjori volcani-sedimentary sequence with quartzite–polymictic conglomerate at its base, disconformably overlies the QPCD and non-conformably over the Mayurbhanj Granite. MG shows the impression of acid magmatic event and also intrudes PGAU (Acharyya et al., 2010). The fact that MG intrudes both QPCD and PGAU is observed from Fig. 8a where it is observed that a resistive feature, which develops from the surface within MG spreads laterally into the QPC and PGAU moving downwards. Conductive zone C2 is observed at the margin of Dhanjori Volcanics and QPCD. This conducting zone lies within the Dhanjori Basin. Alvi and Raza (1992) and Mazumder and Sarkar (2004) explained Dhanjori basin as a volcanosedimentary depository and it overlies unconformably the eroded surfaces of the Singhbhum Granite Complex and the associated older supracrustals, OMG and IOG (Sarkar and Saha, 1962, 1963; Acharyya et al., 2010). This is evident from Fig. 8a where conducting zone C1 overlies the resistive feature R4. The alternate very high resistors (R1 and R3) and moderate resistors (R2) (Fig. 8a) may be explained through various episodes of volcanism in the area.

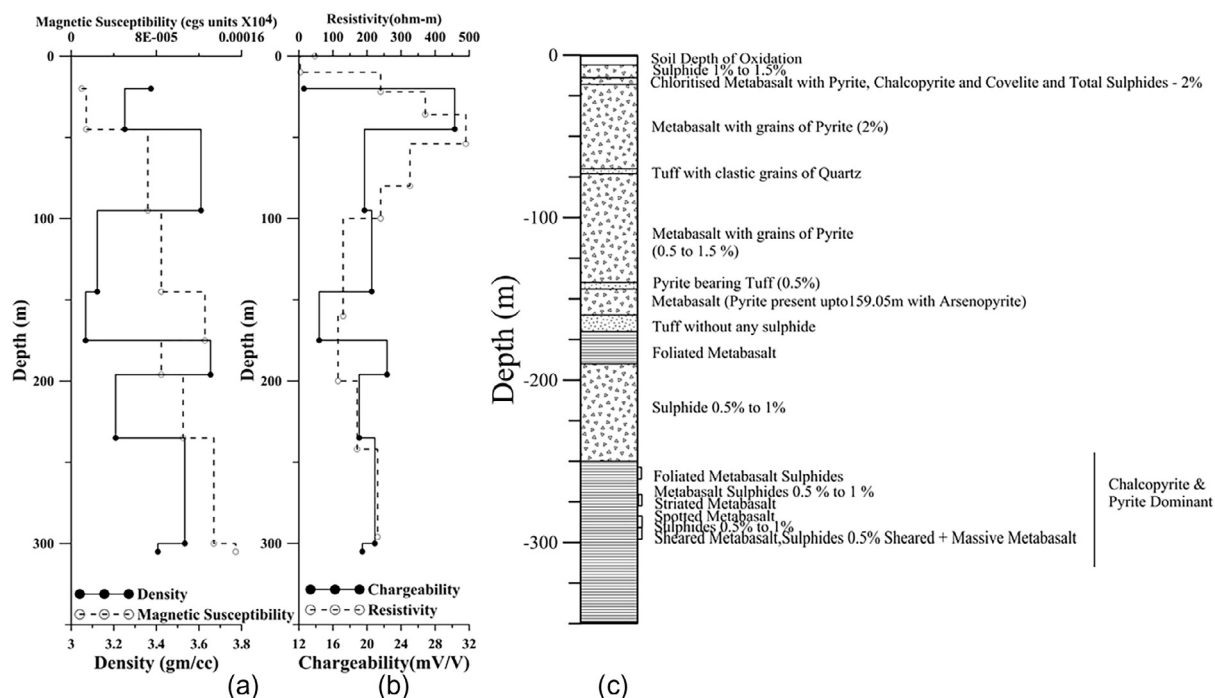Fig. 8b is a magnified model extracted from Fig. 8a, extends to a

Fig. 10. Combined step plot for measured density, susceptibility and chargeability of the core samples at representative depth shown by filled circle, resistivity vs depth section obtained after extracting the resistivity values from the 3-D model from the cells below the borehole data, litholog from borehole (after Das et al., 2008).
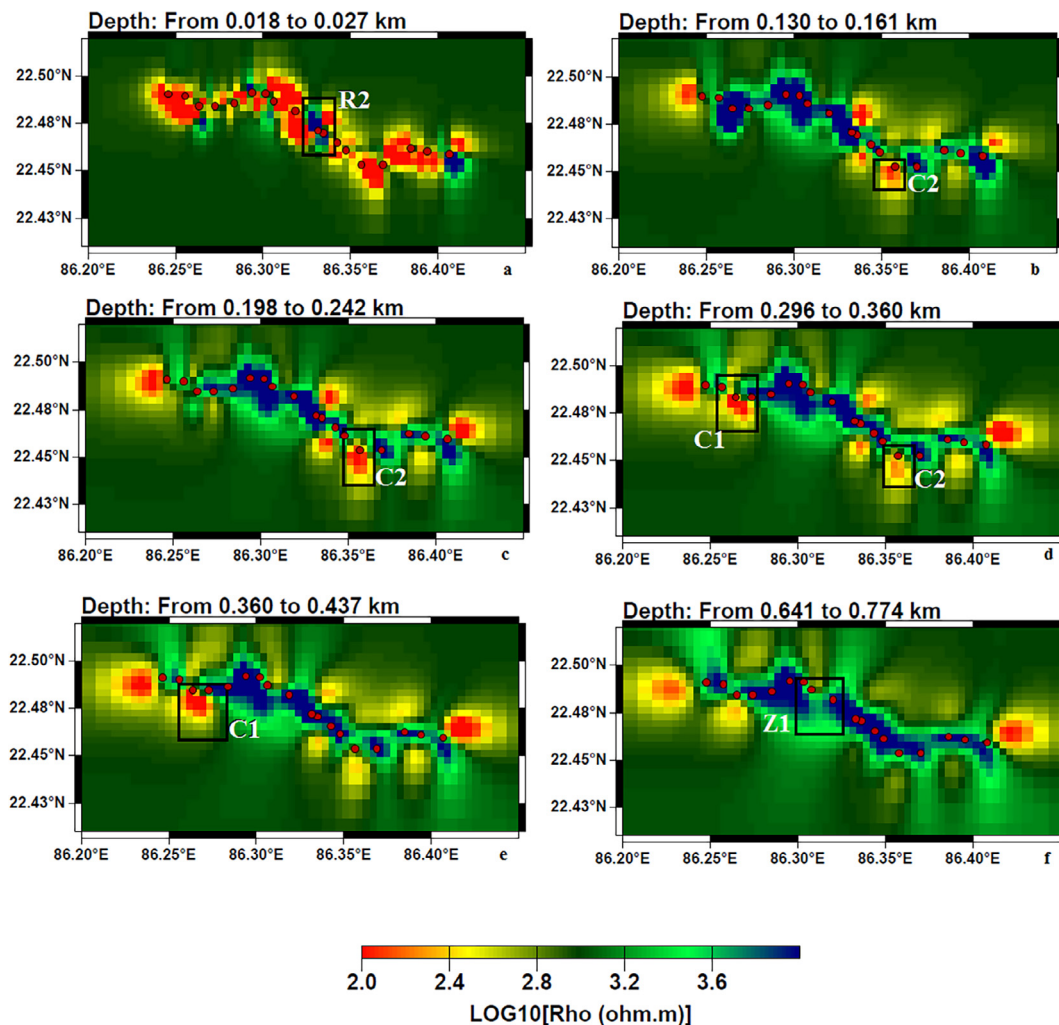
Fig. 11. Horizontal depth slice at various depths: a) 0.018–0.027 km; b) 0.130–0.161 km; c) 0.198–0.242 km; d) 0.296–0.360 km; e) 0.360–0.437 km; f) 0.641–0.774 km. R2, C1, C2 and Z1 are important features and explained in the text.

depth of 800 m. There is a presence of near surface conductor all along the profile extending to a maximum depth of 50 m. This in general, is underlain by a resistive feature. This can be attributed to Dhanjori volcani-sedimentary sequence with quartzite-polymictic conglomerate at its base, disconformably overlies the QPCD and non-conformably over Mayurbhanj granite (Acharyya et al., 2010). Dunn and Dey (1942) stated that the Dhanjori sequence also covers the denuded surface of IOG. The average apparent resistivity in area at 10 kHz is 500 Ωm and skin depth will be ~120 m. This gives the depth of maximum eddy currents flow (Weidelt, 1972), or depth of investigation (Spies, 1989), between 40 and 80 m. Thus, the anomalies in the upper 40 m are detected, but their precise geometries are poorly resolved due to lack of high frequencies (Jones and Garcia, 2003). The conductivity-thickness product is poorly resolved and, thus, a less conductive, thicker feature or its converse can not be precluded based solely on inversions of the AMT data. To resolve these features we compare AMT conductivity model (Fig. 9a) with an electrical resistivity tomography (ERT) section (Fig. 9b) (Gupta et al., 2018) shown by red triangle in Fig. 1. They conducted ERT survey using dipole – dipole array with 10 m electrode spacing and for a profile length of ~1.2 km. The inverted model section of the ERT data (Fig. 9b) shows the presence of shallow conducting feature extending to a depth of ~20 m, can be observed all along the ERT profile. This corroborates well with the AMT results (Fig. 9a) and with bore hole (B1, Fig. 10) confirms the shallow conducting feature. We also find that in both the inverted ERT section and AMT model the

shallow conductors are underlain by highly resistive feature (Fig. 9). The model parameters such as resistivity and depths obtained from ERT and AMT results are comparable for upper uniform shallow conducting feature (< 100 Ωm, 20 m) and underlain resistive feature (< 2000 Ω m).

ERT results shows two more conductors of lateral extent of ~150 m at depth of 50 m while the second conductor of lateral extent of ~80 m at a depth of 50 m. The dimension of these two conductors is very small in comparison to the AMT site spacing (~1km) so these conductors are not mapped in AMT model.

A conducting zone C2 extending from ~100 m to ~300 m close to 03 is observed (Fig. 8). The width of the conductor is more than half of the site spacing and is sufficient enough for its detection in terms of spatial resolution (Queralt et al., 2007). Das et al. (2008) stated the presence of a near vertical conductive body (80 Ωm) adjacent to site 03. The dominant mineral constituent is quartz, which occurs both as clastic grains as well as in matrix making it less conducting in comparison to massive sulfides. Das et al. (2008) measured the density, magnetic susceptibility and chargeability of the core samples at various depths. These have been shown as a step plot of physical property versus depth in Fig. 10. 1-D resistivity variation have been extracted from the model (Fig. 8) beneath the site 03 and shown as a step plot (Fig. 10) extending to the depth of drill hole. The near surface resistivity is ~80 Ωm and increases to about 500 Ωm at a depth of about 50 m. Subsequently, the resistivity falls and reaches a minimum of
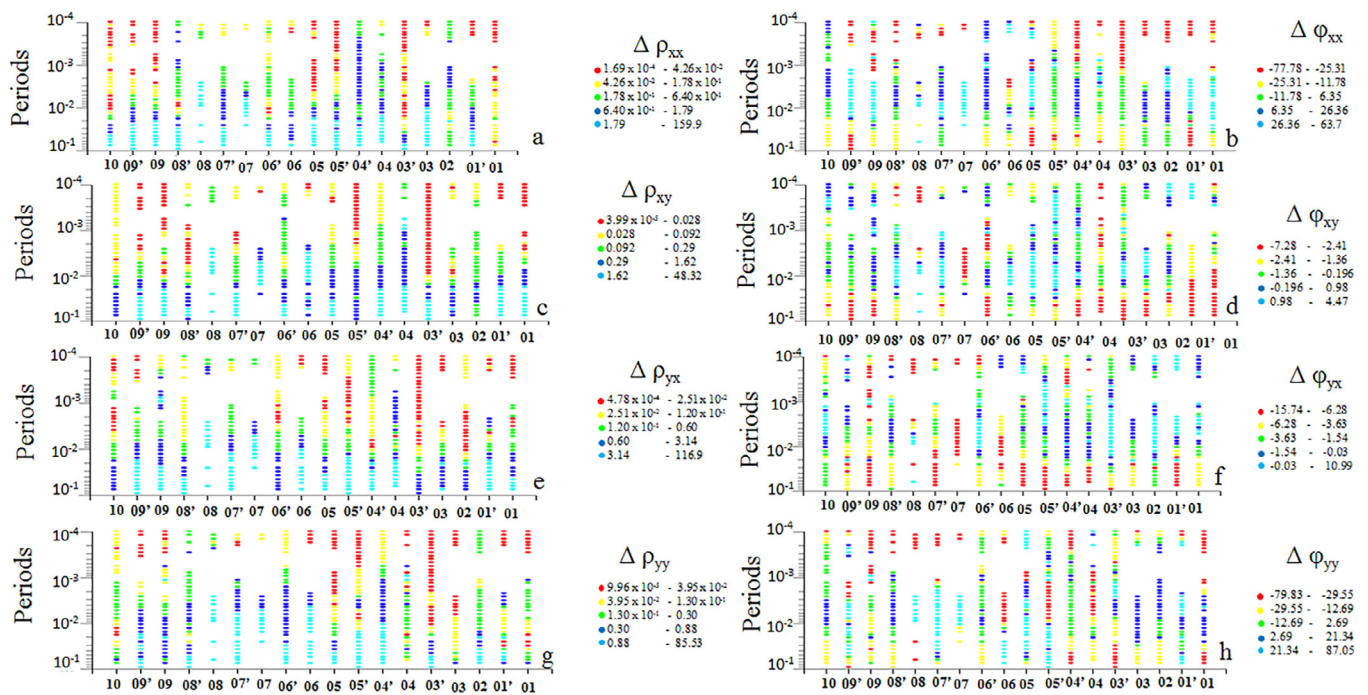
Fig. 12. Pseudo section plot for the misfit between the observed and predicted data for all the sites: a) Δ ρxx; b) Δ Φxx; c) Δ ρxy; d) Δ Φxy; e) Δρyx ; f) ΔΦyx ; g) Δ ρyy; h) Δ Φyy.
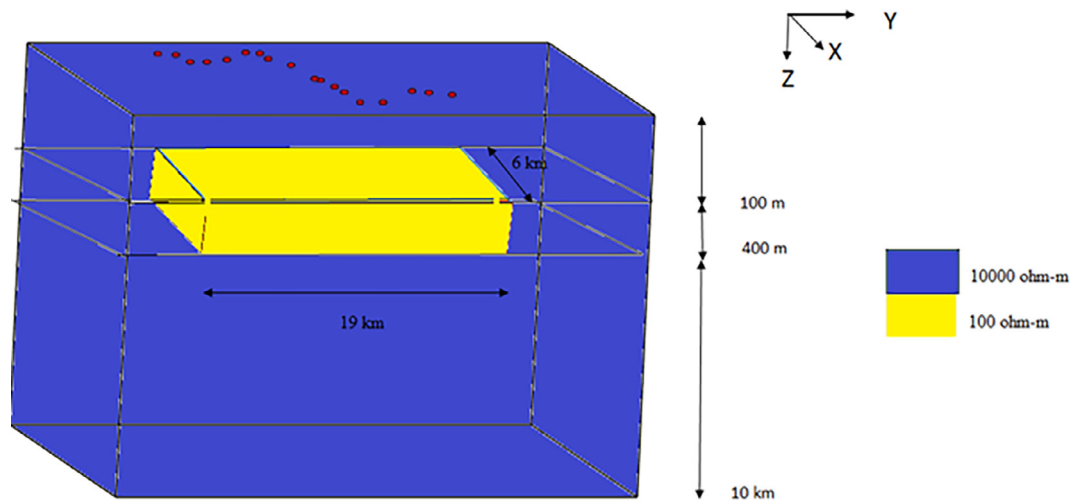

Fig. 13. Synthetic model along with the conductive block. The resistivity of the background block is 10,000 Ωm and resistivity of the main conductive block is 100 Ω m.

~80 Ωm at a depth of about 150 m and increases thereafter. Fig. 10 shows a good correlation with the available litholog. The conducting features (Fig. 8b) at shallow depth which lies all along the profile is attributed to sulphide mineralization with varying concentration from 1% to 2%. However, a thin layer of ~5 m at the surface is observed in the litholog corresponding to soil, which cannot be resolved. The minimum resistivity low at a depth of 150 m coincides with metabasalts (pyrite present up to 159 m with arsenopyrite) (Fig. 10).

In general, low magnetic susceptibility (Fig. 10a) and high chargeability (Fig. 10b) is an indication of metabasalts and sulphide in the study area which is also evident from the borehole (Fig. 10c). Low resistivity for depth less than 20 m corresponds to soil depth of oxidation. The chloritised metabasalt present at depth of 20 m accounts for low magnetic susceptibility whereas the presence of sulphide with 2% concentration increases both the chargeability and density at this depth. The presence of tuff with clastic grains of quartz at depth of

~50 m increases the value of resistivity to 500 ohm-m (Fig. 10b) which is also reflected by high chargeability and low density. The metabasalts (pyrite present with arsenopyrite) at depth of 159 m is well reflected in the resistivity value ~100 ohm-m (Fig. 10b).

Another conducting zone (C1) which appears which appears at 200 m and extends to a depth of ~500 m is observed within the IOG volcanics (Fig. 8b). It is interesting to note that within the IOG there exists Kundarkocha gold mine, borehole B2 (Fig. 1) which is hosted by sheared quartz-carbonate-sulfide veins and is emplaced within the graphitic schist, carbonaceous phyllite and talc–chlorite–serpentine schist. Both lithological and structural factors control gold mineralization in the area (Sahoo and Venkatesh, 2015). They performed detailed ore microscopic studies of the samples collected from Kundarkocha and explained the occurrence of gold as three distinct forms and has a very close relationship with pyrite, arsenopyrite, loellingite and pyrrhotite. Geological Survey of India (GSI) reports that the extension of the veins
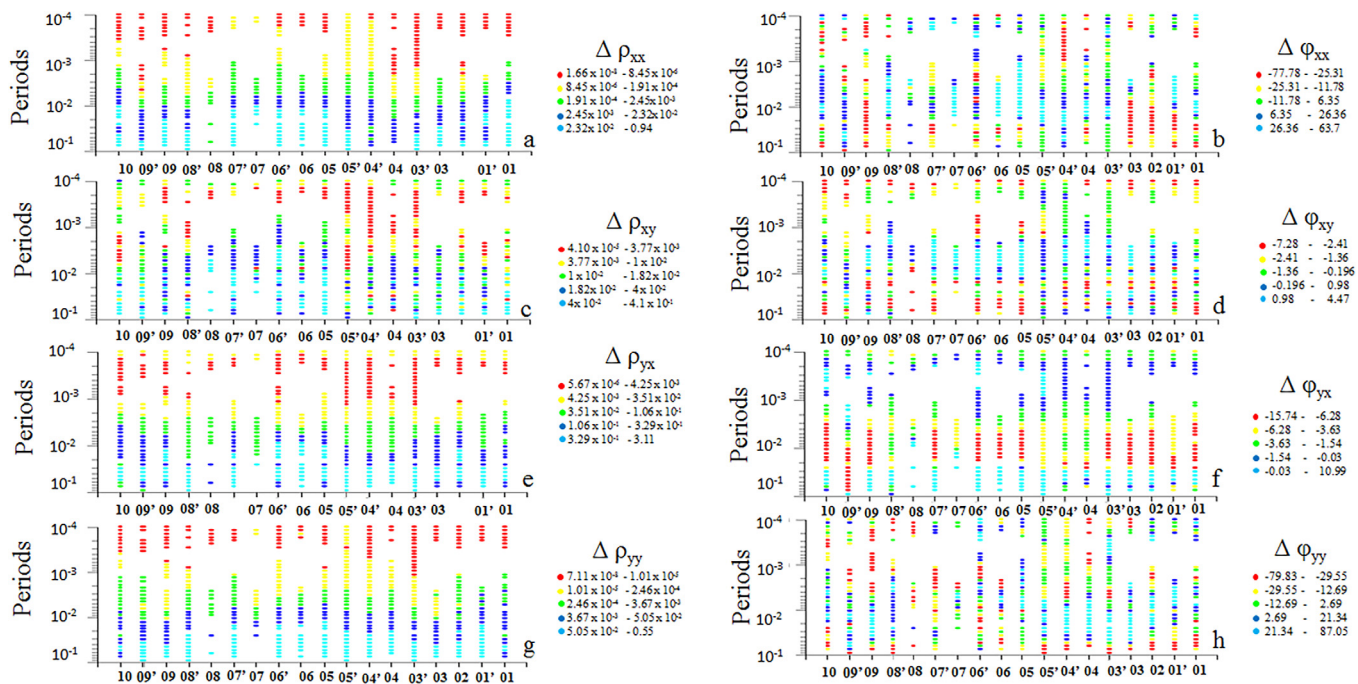
Fig. 14. Pseudo section plot for the observed and predicted data obtained after inverting the data obtained from forward modelling of the synthetic model discussed in Fig. 13. In the figure a) Δ ρxx; b) Δ Φxx; c) Δ ρxy; d) Δ Φxy; e) Δρyx ; f) ΔΦyx ; g) Δ ρyy; h) Δ Φyy.
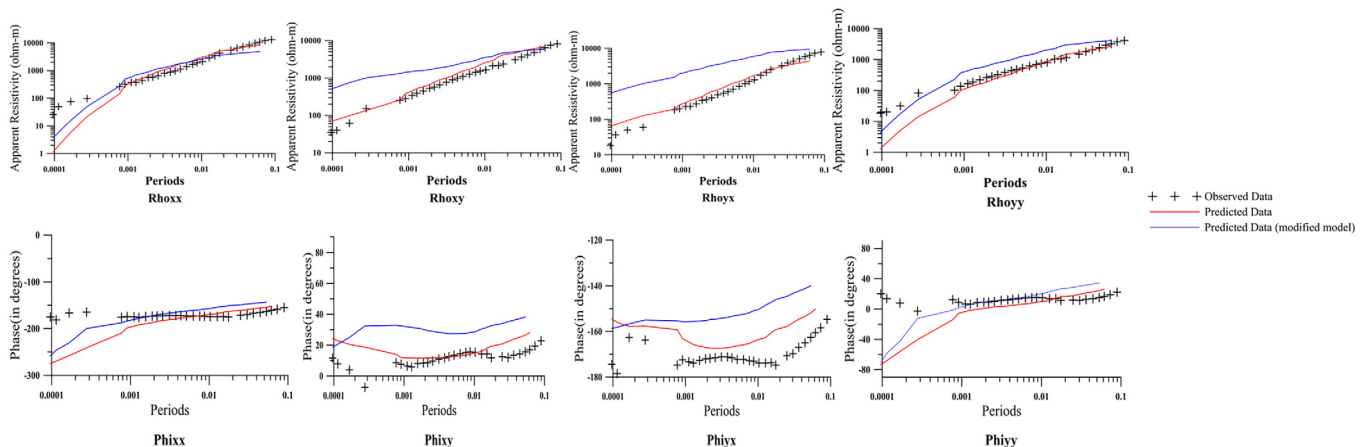

Fig. 15. Sensitivity test result for AMT site 03 over Dhanjori Volcanics. Apparent resistivity and phase responses for all four components of impedance tensor i.e., XX (a), XY (b), YX (c) and YY (d) respectively.

is more in the dip direction as compared to the strike direction and the mineralized veins were traced for about 200 m of the strike length. Total geological reserve calculated is around 63,600 tonnes for two lodes; each of strike length of 250 m extends to a depth of 120 m and average thickness of 0.8 m (Sahoo and Venkatesh, 2015).

The depth slice shows that the resistive feature (R2) within MG starts appearing at a depth of 20 m (Fig. 11a). The off-profile conductor C2 starts appearing from 130 m and extends to a depth of 360 m (Fig. 11b, c, d). Another off-profile conducting feature C1 appears at a depth of 360 m and extends to a depth of ~ 775 m (Fig. 11e, f). In both DhV and IOG, AMT sites are located in the northern extreme so the conductors C1 and C2 were expected towards the south of this profile and it can also be seen from the depth slices (Fig. 11b–f). These depth slices clearly suggest that both the conductors extends towards the south of the profile but exact extension of them cannot be determined accurately only by single AMT profile. There is also a presence of resistive features mostly close to the profile all along the profile (Fig. 11b–d). Further, the presence of linear and continuous resistive

feature, which appears at 130 mm, extends to 640 m, and seems splitting thereafter below MG by a moderate resistor Z1. This resistor can be linked with QPC beds and is overlain by MG and possibly underlain by SG. Following, Cherevatova et al. (2015) we calculated the data misfit between the resistivity and phase data and plotted as a pseudo section (Fig. 12). It is evident that a good match between observed and predicted diagonal and off-diagonal components of apparent resistivity and phase data is seen (Fig. 12). However, for all sites at longer period a relatively large mismatch is seen in all the components of phase data. We performed synthetic tests to evaluate this mismatch.

We simulated a model (Fig. 13) similar to the obtained model (Fig. 8). Synthetic model was considered with 35, 70 and 100 cells in x, y and z directions with the cell dimension along x and y direction to 0.4 km each whereas the cell dimension along z-direction was 0.005 km. In a rather resistive host rock of 10,000 Ωm, a regional block conductor of 100 Ωm with a dimension of 6 km × 19 km × 300 m was embedded at a depth of 100 m (Fig. 13). In other words, the resistivity contrast ratio is 1:100 between the conductor and host rock. AMT data
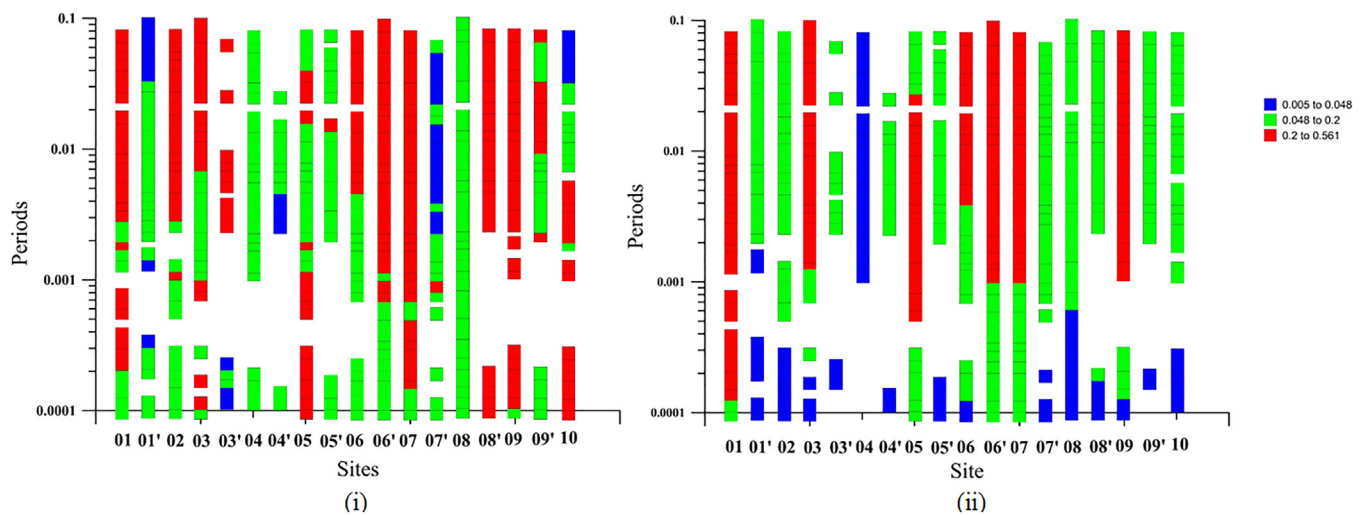
Fig. 16a. Swift skew in frequency range 10 kHz–10 Hz for (i) for observed data; (ii) for modelled data with the inversion result shown in Fig. 8.
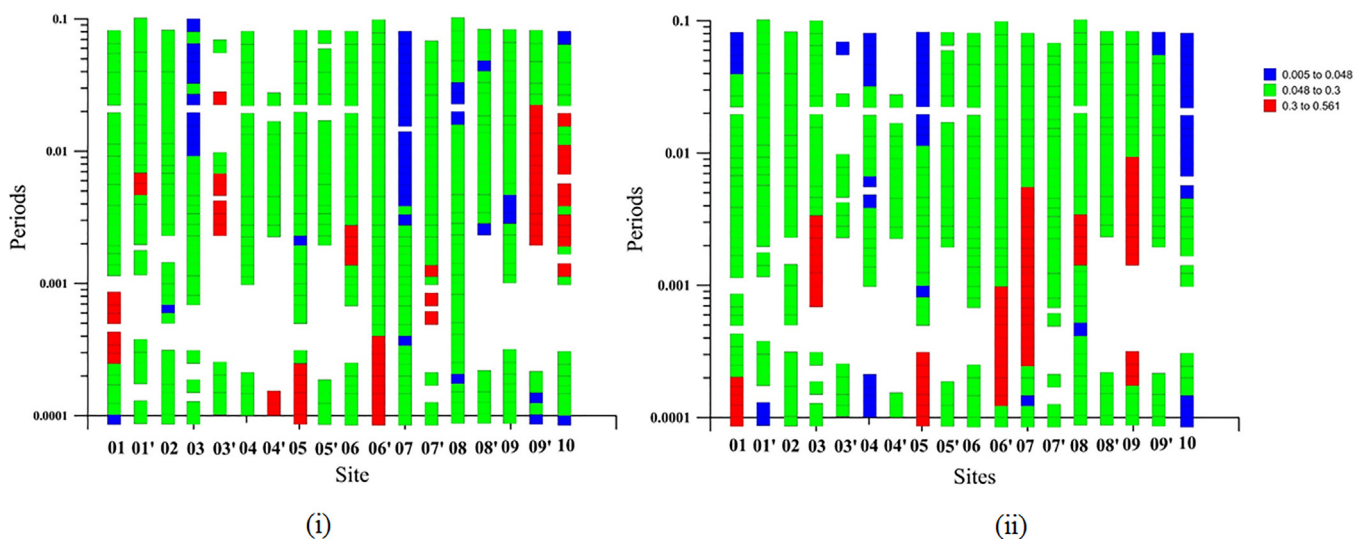

Fig. 16b. Phase sensitive skew in frequency range 10 kHz–10 Hz for (i) observed data; (ii) modelled data with the inversion result shown in Fig. 8.

was generated for the model using forward computation and were subsequently inverted using Modular system for Electromagnetic Inversion (ModEM) for the frequency range of 10 kHz − 10 Hz for the AMT sites layout similar to field (Figs. 1a, 1b).

Pseudosection plot (Fig. 14) shows that although a good match is obtained for all the components of apparent resistivity but phase data shows larger mismatch. The observations are similar to those obtained for field data (Fig. 12). We performed similar exercise with resistivity contrast of 1:1000 and 1: 10 keeping other model parameters same as Fig. 13. All components of apparent resistivity shows good match for both the contrast. A larger mismatch on all the phase component was observed with resistivity contrast of 1:1000 but resistivity contrast of 1:10 resulted in good match all the components of phase data. Thus, a larger mismatch in phase data (Fig. 12) may be attributed to large resistivity contrast.

We performed sensitivity tests for an off-profile conducting model feature lying below site 03. This feature is also seen in the borehole B1 resistivity log and are interpreted as disseminated sulfides in the core samples from the borehole. We replace this off-profile conductor with a moderate resistor of ∼500 ohm-m and the predicted responses for this model feature perturbation are shown in Fig. 15. RMS fit for site 03 increases from 2.15–6.73 after model perturbation, which also confirms that the obtained model (Fig. 8) needs this feature to explain the data

fits.

Swift skew (Fig. 16a) and PSS (Fig. 16b) has been evaluated for the modelled data and has been compared with that of the observed data. Fig. 16 clearly suggests that the dimensionality values for both swift skew and PSS matches well in both the cases (Fig. 16a, b) for most of the sites with exception at few periods.

Fig. 17 shows comparison of the earlier 2D results (Singh et al., 2018) (Fig. 17a) with the present 3D model (Fig. 17b). The 2D model (Singh et al., 2018) have been redrawn for comparison with the 3D model. Conductor 'C1′ at the boundary of IOG and PGAU is marked by both 2D and 3D models but the 3D model shows highly resolved localized dimension of C1 whereas in 2D model it is widely distributed. There is a presence of thin resistive layer above the conductor 'C1′ in the 3D model which is not observed in the 2D model because the higher frequencies ranging between 10 kHz and 1 kHz was not used in the 2D inversion study of Singh et al. (2018). Conductor 'C2′ below DhV is well resolved in the 3D model. In general, depth to the base of the main conducting features observed in 3-D models is underestimated as compared to the 2D models. The moderately resistive feature 'Cq' with 500–2000 ohm-m resistivity in the 2D model appears at a shallower depth in the 3D model (here renamed as R2) consistent with Ledo (2005). This feature appears much more localized along the profile direction in 3D model as compared to the 2D model. The resistive MG
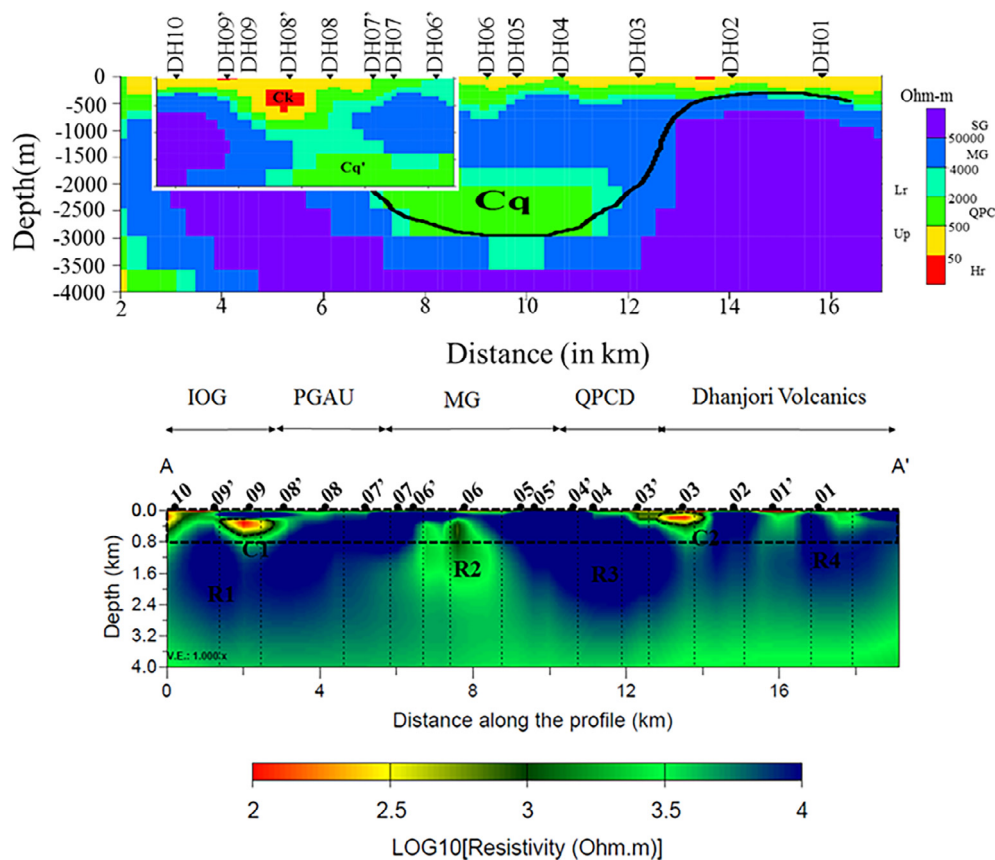
Fig. 17. Comparison of 2D model (taken from Singh et al., 2018) with the present 3D model (shown in Fig. 8).
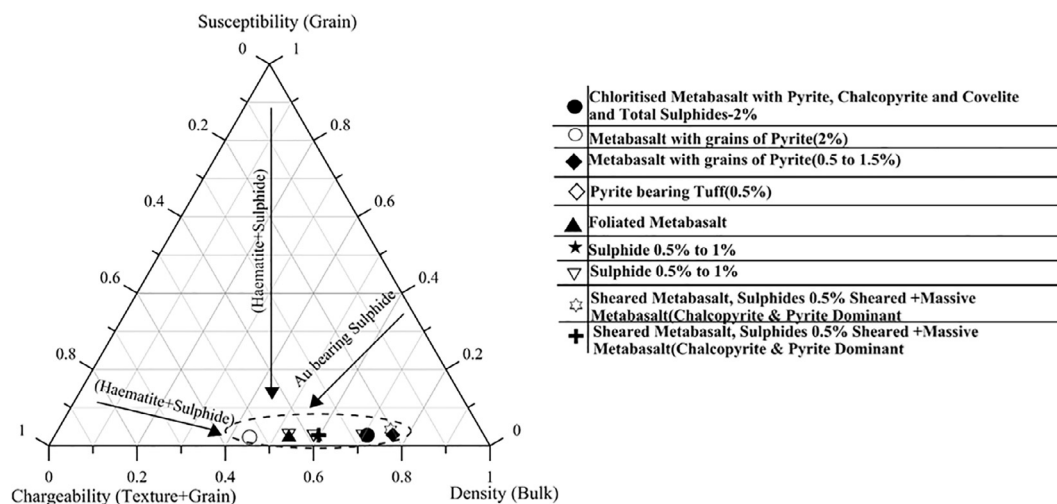

Fig. 18. Ternary diagram showing the relative influence of measured physical properties density, chargeability and susceptibility of core samples on petrophysical properties texture, grains and bulk properties.

appears both in 2D and 3D models but in case of 3D model, it is well connected overlying the moderately resistive QPCD unlike the 2D model.

6. Petrophysical characterization

Das et al. (2008) measured density, susceptibility and chargeability of the core samples from the borehole and is shown as a step plot in Fig. 10. Using these, we try to comment on metamorphism/serpentenization and petrophysics using Henkel, combined scatter and component proportional phase and ternary plots respectively in the study area.

On comparison of density, susceptibility and chargeability data of core samples with litholog (Fig. 10) it is observed that high density, high chargeability and negligible susceptibility corresponds to metabasalts with grains of pyrites. Low density, negligible susceptibility and low chargeability at a depth of 175 m correspond to foliated metabasalts. The sulphides varying in concentration from 0.5% to 1% shows high density, high chargeability and negligible susceptibility (Parasnis, 1956; Johnson and Anderson, 1981). The foliated metabasalts with dominance of chalcopyrite and pyrite at depth of 300 m shows high density, high chargeability and negligible susceptibility.

The low susceptibility and high density indicates that the study area is of low-grade green schist metamorphic facies, which corresponds with the geological stratigraphy of the area. Further, the density and susceptibility data when plotted on Henkel plot shows that the host rock occupies paramagnetic field, and it indicates lower degree of serpentenization (Dentith and Mudge, 2014). The results further suggest that the lithotypes are similar to those of granitoid-greenstone terrain in the Abitibi Subprovince (Dentith and Mudge, 2014).

Based on magnetic susceptibility and density data, Hanneson (2003) classified the rock forming minerals in three broad categories: 1) magnetite, 2) hematite and sulphides, and 3) barren host rock. The high density and low susceptibility has been categorised as haematite + sulphide. They used combined phase and scatter diagram to relate petrophysical measurements on a rock specimen to its mineral category content. Plotting the susceptibility and density data on their combined phase and scatter diagram the obtained values for haematite + sulphide, magnetite and barren host rock are 20 vol%, 2 vol% and 78 vol% respectively. However, their diagram does not consider the physical property chargeability, which can distinguish between haematite and sulphide and whether the sulphide is massive or disseminated. Haematite and massive sulphides show negligible chargeability whereas the chargeability of disseminated sulphide is at higher side. Fig. 10 shows that in the study area, chargeability is high and susceptibility is negligible, thus, 20 vol% are predominantly disseminated sulphide and not haematite + sulphide. Following, Nelson and Van Voorhis (1983) the estimated conductivity of the sulphides is 0.16 mho/m for 20 vol% which further ascertains that the sulphides are disseminated type.

The petrophysical property could be quantified by the study of texture, grain and bulk properties of the host rock. Bulk properties are the weighted average of the constituent mineral properties. Grain properties depend on minority component of the rock, which may make up only a few percent of the total mineralogy. They are controlled by both the abundance of the relevant minerals and the texture of the grains. The texture property depends mainly on the texture of the rock. Density, susceptibility and chargeability are the bulk, grain and texture and grain properties of mineral respectively (Dentith et al., 2017). Ternary diagram (Fig. 18) with end members as chargeability (texture + grain), susceptibility (grain) and density (bulk) shows the relative influence of texture, grains and bulk effects on mineral properties. The gold bearing sulphide mineralization of the study area is being controlled by texture and grain properties.

7. Summary and conclusion

The present work discusses the conductivity model from 3-D inversion of AMT data for regional mapping and associated mineralization. In addition, a petrophysical interpretation has been carried out by linking geological set up, resistivity sections and physical properties of the core samples that can influence the mineralization. The study area represents a typical greenstone belt meta-volcano-sedimentary sequence within the Singhbhum Crustal Province, lying in the Eastern part of India. Gold mineralization within the study area i.e., Dhanjori Formation is confined to the mafic/ultramafic meta-volcanic rocks as lode gold and also as placer gold within the QPCD.

The data analysis suggested the area to be complex and thus 3-D inversion was performed. The 3-D conductivity model maps the regional resistive features as well as shallow conducting features. The mapped regional features corroborates well with the regional geology. The conductivity model shows the presence of alternate zones of high and moderate resistivity. This may be due to different episodes of volcanism in the area. The sediments and the fluids can account for the shallow conductor within the Dhanjori volcanics matches well with the available borehole data. Interestingly, all along the profile a near surface conductor is mapped. These results when compared with available ERT section in QPCD confirm the presence of shallow conductors. This near surface conductor is attributed to Dhanjori volcano-sedimentary sequence with quartzite-polymictic conglomerate. To understand the physical properties of rocks in mineralized geological environment as mapped by AMT method, petrophysical study have been attempted. It helps in accurately mapping the geology, which are equally dependent on petrophysics. The petrophysical studies helped us to estimate the concentration of minerals within the rocks. The Henkel plot between density and susceptibilities confirms that the study area shows low-grade metamorphism and low level of serpentenization. When these data were plotted on combined phase and scatter diagram, it indicates that haematite + sulphide has 20 vol% contribution. The available high chargeability data of the core samples suggested that 20 vol% is from disseminated sulphide only. The ternary diagram suggests that mineralization is primarily influenced by texture and grain properties. Petrophysical analysis suggests that the lithotypes of the study area are similar to those of greenstone terrain in the Abitibi Subprovince. Infact, the petrophysical studies should be performed on the outcrops as a reconnaissance study. This can easily predict the mineralization prospect over an area. Further, the non-uniqueness inherent in geophysical exploration can be substantially reduced by integrating geology, electrical conductivity models and petrophysical properties. Considering all points together the study of integrating AMT with petrophysics for deeper deposits has a substantial impact on the study area and indeed provides a new orientation and advancement to the exploration strategy.

Acknowledgements

Appendix A. Supplementary data

Supplementary data to this article can be found online at https://doi.org/10.1016/j.oregeorev.2019.01.027.

References

Acharyya, S.K., Gupta, A., Orihashi, Y., 2010. Neoarchean-Paleoproterozoic stratigraphy of the Dhanjori basin, Singhbhum Craton, Eastern India: and recording of a few U-Pb zircon dates from its basal part. J. Asian Earth Sci. 39, 527–536.

Alvi, S.H., Raza, M., 1992. Geochemical evidence for the volcanic arc tectonic setting of the Dhanjori volcanics, Singhbhum Craton, eastern India. Geol. Mag. 129, 337–348.

Bahr, K., 1991. Geological noise in magnetotelluric data: a classification of distortion types. Phys. Earth Planet. Inter. 66, 24–38.

Bandopadhyay, P.C., Sengupta, S., 2004. The paleoproterozoic supracrustal Kolhan group in Singhbhum craton, India and the Indo-African supercontinent. Gondwana Res. 7, 1228–1235.

Banerji, A.K., 1969. A reinterpretation of the geological history of the Singhbhum Shear Zone. Bihar Geol. Soc. India J. 15, 49–55.

Banerji, A.K., 1977. On the Precambrian banded iron-formations and the manganese ores or the Singhbhum region, eastern India. Econ. Geol. 72, 90–98.

Banerjee, P.K., 1977. Stratigraphy, petrology and geochemistry of some Precambrian basic volcanic and associated rocks of Singhbhum district, Bihar and Mayurbhanj and Keonjhar districts, Orissa. Geol. Surv. India, Mem. v (111), 58.

Basu, A., 1985. Structure and stratigraphy in and around S.E.—Part of Dhanjori Basin, Singhbhum. Bihar. Rec. Geol. Surv. India 113, 59–67.

Berdichevsky, M.N., Zhdanov, M.S., 1984. Advanced Theory of Deep Geomagnetic Sounding (No. 19). Elsevier Science Ltd.

Berdichevsky, M.N., Dmitriev, V.I., Pozdnjakova, E.E., 1998. On two-dimensional interpretation of magnetotelluric soundings. Geophys. J. Int. 133, 585–606. https://doi.org/10.1046/j.1365-246X.1998.01333.x.

Berdichevsky, M.N., 1999. Marginal notes on magnetotellurics. Surv. Geophys. 20, 341–375.

Bibby, H.M., Caldwell, T.G., Brown, C., 2005. Determinable and non-determinable parameters of galvanic distortion in magnetotellurics. Geophys. J. Int. 163, 915–930.

Brasse, H., Lezaeta, P., Rath, V., Schwalenberg, K., Soyer, W., Haak, V., 2002. The Bolivian altiplano conductivity anomaly. J. Geophys. Res. Solid Earth 107. https://doi.org/10.1029/2001JB000391.

Cagniard, L., 1953. Basic theory of the magnetotelluric method of geophysical prospecting. Geophysics 18, 605–645.

Caldwell, T.G., Bibby, H.M., Brown, C., 2004. The magnetotelluric phase tensor. Geophys. J. Int. 158, 457–469.

Chakraborty, K.L., bhattacharya, A., Roy, B., 1981. Gabbro- anorthosite-granophyre-leucogranite relationship around Gorumasihani Hill, Mayurbhanj District. Orissa. Jour. Geol. Soc. India 22, 336–341.

Chakravarti, R., Singh, S., Venkatesh, A.S., 2017. Gold mineralisation within quartz pebble conglomerates of gorumahisani-badampahar schist belt, singhbhum craton, Eastern India. J. Geosci. Res. Special Volume, 27–34.

Chave, A.D., Jones, A.G. 2012. The Magnetotelluric Method—Theory and Practice. Cambridge Univ. Press, Cambridge, UK, pp. 570.

Cherevatova, M., Smirnov, M.Y., Jones, A.G., Pedersen, L.B., Becken, M., Biolik, M., Ebbing, J., Gradmann, S., Gurk, M., Hübert, J., Junge, A., Kamm, J., Korja, T., Lahti, I., Lower, A., Nittinger, C., Savvaidis, A., 2015. Magnetotelluric array data analysis from north-west Fennoscandia. Tectonophysics 653, 1–19.

Craven, J.A., Roberts, B.J., Hayward, N., Stefanescu, M., Corriveau, L., 2013. A magnetotelluric survey and preliminary geophysical inversion and visualization of the NICO IOCG deposit, Northwest Territories. Geol. Surv. Can. Open File 7465, 26.

Das, L.K., Dasgupta, K.K., De, M.K., 2008. Mineral potential of Dhanjori Metavolcanics, East Singhbhum, Jharkhand. Indian Minerals 61, 193–200.

Deb, M., 2014. Precambrian geodynamics and metallogeny of the Indian shield. Ore Geol. Rev. 57, 1–28.

Dentith, M., Mudge, S.T., 2014. Geophysics for the Mineral Exploration Geoscientist. Cambridge University Press.

Dentith, M., Adams, C., Bourne, B., Petrophysics and Exploration Targeting: Best Practice and Applications. http://www.terrapetrophysics.com.au/wp-content/uploads/2017/05/Dentith-et-al-Target2017_Abstract_v1.pdf.

Dunn, J.A., Dey, A.K., 1942. The geology and petrology of Eastern Singhbhum and surrounding areas. Mem. Geol. Surv. India 69, 281–456.

Egbert, G.D., Kelbert, A., 2012. Computational recipes for electromagnetic inverse problems. Geophys. J. Int. 189, 251–267. https://doi.org/10.1111/j.1365-246X.2011.05347.x.

Eriksson, P.G., Mazumder, R., Sarkar, S., Bose, P.K., Altermann, W., Van Der Merwee, R., 1999. The 2.7–2.0 Ga volcanosedimentary record of Africa, India and Australia: evidence for global and local changes in sea level and continental freeboard. Precambr. Res. 97, 269–302.

Gamble, T.D., Goubau, W.M., Clarke, J., 1979a. Magnetotellurics with a remote reference. Geophysics 44, 53–68.

Gamble, T.D., Goubau, W.M., Clarke, J., 1979b. Error analysis for remote reference magnetotellurics. Geophysics 44, 959–968.

Garcia, X., Ledo, J., Queralt, P., 1999. 2D inversion of 3D magnetotelluric data. Earth Planets Space 51, 1135–1143. https://doi.org/10.1186/BF03351587.

Ghose, N.C., 1996. Gold occurrences and its potentiality in Bihar. In: Preworkshop volume on Gold resources of India held during Dec 2–4, 1996. Organized by Geological Society of India and National Geophysical Research Institute, Hyderabad, pp. 214–227.

Groves, D.I., Phillips, G.N., Ho, S.E., Houstoun, S.M., Standing, C.A., 1987. Craton-scale distribution of Archean greenstone gold deposits; predictive capacity of the metamorphic model. Econ. Geol. 82, 2045–2058. https://doi.org/10.2113/gsecongeo.82.8.2045.

Gupta, A., Basu, A., Singh, S.K., 1985. Stratigraphy and petrochemistry of Dhanjori greenstone belt, eastern India. Q. J. Geol. Min. Metall. Soc. India 57, 248–263.

Gupta, A., Singh, R.K., Shalivahan, 2018. Investigation of auriferous mineralization over Greenstone Schist Belt of Dhanjori Basin, Eastern India using 2-D ERT and IP surveys (accepted).

Hanneson, J.E., 2003. On the use of magnetics and gravity to discriminate between gabbro and iron-rich ore-forming systems. Explor. Geophys. 34, 110–113.

Haque M.D., Dutta, S.K., 1996. Report On The Investigation For Gold In Dhanjori Basin In East Singhbhum District, Bihar, Unpublished Report, Geological Survey of India.

Hermance, J.F., 1982. The asymptotic response of three-dimensional basin offsets to magnetotelluric fields at long periods: the effects of current channeling. Geophysics 47, 1562–1573. https://doi.org/10.1190/1.1441306.

Heinson, G.S., Direen, N.G., Gill, R.M., 2006. Magnetotelluric evidence for a deep-crustal mineralizing system beneath the Olympic Dam iron oxide copper-gold deposit, southern Australia. Geology 34, 573–576. https://doi.org/10.1130/G22222.1.

Hersir, G.P., Árnason, K., Vilhjálmsson, A.M., 2013. In: 3D Inversion of Magnetotelluric (MT) Resistivity Data from Krýsuvík High Temperature Geothermal Area in SW Iceland. Stanford Univ, Stanford, pp. (p. 14)..

Huber, P.J., 1981. Robust Statistics. John Wiley, Hoboken, NJ.

Ichihara, H., Mogi, T., Uyeshima, M., Sakanaka, S., 2010. Three dimensional conductor models explaining out of quadrant magnetotelluric phases, IAGA WG 1.2 on Electromagnetic Induction in the earth, 20th workshop abstract, Giza, Egypt, September 18–24.

Iyenger, S.V.P., Alwar, M.A., 1965. The Dhanjori eugesyncline and its bearing on stratigraphy of Singhbhum, Keonjhar and Mayurbhanj districts. D.N. Wadia Commem. Vol. Min. Geol. Met. Inst. India 138–162.

Jayananda, M., Peucat, J.-J., Chardon, D., Krishna, Rao B., Corfu, F., 2013. Neoarchean greenstone volcanism, Dharwar craton, Southern India: constraints from SIMS zircon geochronology and Nd isotopes. Precambr. Res. 227, 55–76. https://doi.org/10.1016/j.precamres.

Johnson, G.R., Anderson, L.A., 1981. A laboratory study of some physical properties of sulfide ores in igneous and metamorphic rocks from the Burnt Nubble area, Somerset County, Maine (No. 81-669). US Geological Survey.

Jones, F.W., Vozoff, K., 1978. The calculation of magnetotelluric quantities for three-dimensional conductivity inhomogeneities. Geophysics 43, 1167–1175. https://doi.org/10.1190/1.1440886.

Jones, A.G., 1983. The problem of current channelling: a critical review. Surv. Geophys. 6, 79–122.

Jones, A.G., Garcia, X., 2003. Okak Bay AMT data-set case study: lessons in

dimensionality and scale. Geophysics 68, 70–91. https://doi.org/10.1190/1.1543195.

Kaufman, A.A., Keller, G.V., 1981. The magnetotelluric sounding method. Methods in geochemistry and geophysics, 15.

Kelbert, A., Meqbel, N., Egbert, G.D., Tandon, K., 2014. ModEM: a modular system for inversion of electromagnetic geophysical data. Comput. Geosci. 66, 40–53. https://doi.org/10.1016/j.cageo.2014.01.010.

Koziar, A., Strangway, D.W., 1978. Shallow crustal sounding in the Superior Province by audio frequency magnetotellurics. Can. J. Earth Sci. 15, 1701–1711. https://doi.org/10.1139/e78-180.

Ledo, J., 2005. 2-D versus 3-D magnetotelluric data interpretation. Surv. Geophys. 26, 511–543.

Livelybrooks, D., Mareschal, M., Blais, E., Smith, J.T., 1996. Magnetotelluric delineation of the Trillabelle massive sulfide body in Sudbury, Ontario. Geophysics 61, 971–986. https://doi.org/10.1190/1.1444046.

Mahadevan, T.M., 2002.Geology of Bihar and Jharkhand. Geological Society of India, 563.

Marti, A., Queralt, P., Ledo, J., 2009. WALDIM: a code for the dimensionality analysis of magnetotelluric data using the rotational invariants of the magnetotelluric tensor. Comput. Geosci. 35, 2295–2303.

Mazumder, R., 2002. Sedimentation history of the Dhanjori and Chaibasa formations, eastern India and its implications.   Unpublished Ph.D. thesis. Jadavpur University, pp. 119.

Mazumder, R., 2003. Correlations between the Eastern Block of the North China Craton and the South Indian Block of the Indian Shield: an Archaean to Palaeoproterozoic link—comment. Precambr. Res. 127, 379–380.

Mazumder, R., 2005. Proterozoic sedimentation and volcanism in the Singhbhum crustal province, India and their implications. Sed. Geol. 176, 167–193. https://doi.org/10.1016/j.sedgeo.2004.12.011.

Mazumder, R., Bose, P.K., Sarkar, S., 2000. A commentary on the tectono-sedimentary record of the pre-2.0 Ga continental growth of India vis a vis a pre-Gondwana Afro-Indian supercontinent. J. Afr. Earth Sci. 30, 201–217.

Mazumder, R., Sarkar, S., 2004. Sedimentation history of the Palaeoproterozoic Dhanjori Formation, Singhbhum, eastern India. Precambr. Res. 130, 267–287.

Meju, M.A., 2002. Geoelectromagnetic exploration for natural resources: models, case studies and challenges. Surv. Geophys. 23, 133–206. https://doi.org/10.1023/A:1015052419222.

Meqbel, N.M., Egbert, G.D., Wannamaker, P.E., Kelbert, A., Schultz, A., 2014. Deep electrical resistivity structure of the northwestern U.S. derived from 3-D inversion of US Array magnetotelluric data. Earth Planet. Sci. Lett. 402, 290–304.

Misra, S., Johnson, P.T., 2005. Geochronological constraints on evolution of Singhbhum mobile belt and associated basic volcanics of eastern Indian shield. Gondwana Res. 8, 129–142. https://doi.org/10.1016/S1342-937X(05)71113-8.

Nelson, P.H., Van Voorhis, G.D., 1983. Estimation of sulfide content from induced polarization data. Geophysics 48, 62–75.

Newman, G.A., Recher, S., Tezkan, B., Neubauer, F.M., 2003. 3D inversion of a scalar radio magnetotelluric field data set. Geophysics 68, 791–802.

Parasnis, D.S., 1956. The electrical resistivity of some sulphide and oxide minerals and their ores. Geophys. Prospect. 4, 249–278.

Park, S.K., Orange, A.S., Madden, T.R., 1983. Effects of three-dimensional structure on magnetotelluric sounding curves. Geophysics 48, 1402–1405. https://doi.org/10.1190/1.1441422.

Park, S.K., 1985. Distortion of magnetotelluric sounding curves by three-dimensional structures. Geophysics 50, 785–797. https://doi.org/10.1190/1.1441953.

Park, S.K., Torres-Verdin, C., 1988. A systematic approach to the interpretation of magnetotelluric data in volcanic environments with applications to the quest for magma in Long Valley, California. J. Geophys. Res. Solid Earth 93, 13265–13283. https://doi.org/10.1029/JB093iB11p13265.

Park, S.K., Mackie, R.L., 2000. Resistive (dry?) lower crust in an active orogen, Nanga Parbat, northern Pakistan. Tectonophysics 316, 359–380. https://doi.org/10.1016/S0040-1951(99)00264-4.

Patro, P.K., Egbert, G.D., 2011. Application of 3D inversion to magnetotelluric profile data from the Deccan Volcanic Province of Western India. Phys. Earth Planet. Inter. 187, 33–46. https://doi.org/10.1016/j.pepi.2011.04.005.

Pirajno, F., 2007. Mantle plumes, associated intraplate tectono-magmatic processes and ore systems. Episodes 30, 6.

Queralt, P., Jones, A.G., Ledo, J., 2007. Electromagnetic imaging of a complex ore body: 3D forward modeling, sensitivity tests, and down-mine measurements. Geophysics 72, F85–F95. https://doi.org/10.1190/1.2437105.

Roy, A., Sarkar, A., Jeyakumar, S., Aggrawal, S.K., Ebihara, M., 2002. Sm–Nd age and mantle characteristics of the Dhanjori volcanic rocks, Eastern India. Geochem. J. 36, 503–518.

Saha, A.K., 1975. The Mayurbhanj granite - A Precambrian batholith in Eastern India. J. Geol. Soc. India 16, 37–43.

Saha, A.K., 1988. Some aspects of crustal growth of the Singhbhum-Orissa Iron Ore craton, eastern India. Ind. J. Geol. 60, 270–278.

Saha, A.K., 1994. M-27. Crustal Evolution of Singhbhum-North Orissa, Eastern India. GSI Publications.

Sahoo, P.R., Venkatesh, A.S., 2015. Constraints of mineralogical characterization of gold ore: implication for genesis, controls and evolution of gold from Kundarkocha gold deposit, eastern India. J. Asian Earth Sci. 97, 136–149.

Sarkar, S.C., 1984. Geology and Ore Mineralisation of the Singhbhum Copper–Uranium Belt, Eastern India. Jadavpur University, Calcutta,pp. pp. 263.

Sarkar, S.N., Saha, A.K., 1962. A revision of the Precambrian stratigraphy and tectonics of Singhbhum and adjacent region. Quart. J. Geol. Min. Metal. Soc. India 34, 97–136.

Sarkar, S.N., Saha, A.K., 1963. On the occurrence of two intersecting Pre-Cambrian

orogenic belts in Singhbhum and adjacent areas, India. Geol. Mag. 100, 69–92. https://doi.org/10.1017/S0016756800055060.

Sarkar, S.N., Saha, A.K., 1977. The present status of the Precambrian stratigraphy, tectonics, and geochronology of Singhbhum-Keonjhar-Mayurbhanj region, eastern India. Indian J. Earth Sci. S. Ray Vol. 37–65.

Sasaki, Y., 2004. Three-dimensional inversion of static-shifted Magnetotelluric data. Earth Planets Space 56, 239–248.

Sasaki, Y., Meju, M.A., 2006. Three-dimensional joint inversion for Magnetotelluric resistivity and static shift distributions in complex media. J. Geophys. Res. 111. https://doi.org/10.1029/2005JB004009.

Shalivahan, Sinharay, R.K., Bhattacharya, B.B., 2006. Remote reference magnetotelluric impedance estimation of wideband data using hybrid algorithm. J. Geophys. Res. 111. https://doi.org/10.1029/2006JB004330.

Simpson, F., Bahr, K., 2005. Practical Magnetotellurics. Cambridge University Press.

Singh, S., Maurya, V.P., Singh, R.K., Tripathi, Shalivahan, A., Adhikari, P.K., 2018. Audio magnetotelluric Investigation of Sulfide Mineralizationin Proterozoic-Archean Greenstone belts of Eastern Indian Craton. J. Earth Syst. Sci. 127, 34. https://doi.org/10.1007/s12040-018-0938-z.

Singh, S.P., 1998. Precambrian stratigraphy of Bihar. In: Paliwal, B.S. (Ed.), The Indian Precambrian. Scientific Publ, Jodhpur, pp. 376–408.

Singh, S.P., Nim, S.P., 1998. Stratigraphy of the lower proterozoic sequence of Patharchakri-Mosaboni area, Singhbhum. Bihar. Indian Min. 52, 1–14.

Siripunvaraporn, W., 2012. Three-dimensional magnetotelluric inversion: an introductory guide for developers and users. Surv. Geophys. 33, 5–27.

Siripunvaraporn, W., Egbert, G., Uyeshima, M., 2005. Interpretation of two-dimensional magnetotelluric profile data with three-dimensional inversion: synthetic examples. Geophys. J. Int. 150, 804–814.

Spies, B.R., 1989. Depth of investigation in electromagnetic sounding methods. Geophysics 54, 872–888.

Stodt, J.A., 1983. Noise Analysis for Conventional and Remote Reference Magnetotellurics. Ph.D. thesis. Univ. of Utah, Salt Lake City.

Swift, C.M., 1967. A Magnetotelluric Investigation of an Electrical Conductivity Anomaly in the South Western United States. PhD Thesis. Massachusetts Institute of Technology.

Takasugi, S., Tanaka, K., Kawakami, N., Muramatsu, S., 1992. High spatial resolution of the resistivity structure revealed by a dense network MT measurement. J. Geomagn. Geoelec. 44, 289–308. https://doi.org/10.5636/jgg.44.289.

Telford, W.M., Telford, W.M., Geldart, L.P., Sheriff, R.E., Sheriff, R.E., 1990. Applied Geophysics. Cambridge University Press.

Tikhonov, A.N., 1950. The determination of the electrical properties of deep layers of the Earth's crust. Dokl. Acad. Nauk. SSR 73, 295–297 (in Russian).

Ting, S.C., Hohmann, G.W., 1981. Integral equation modeling of three-dimensional magnetotelluric response. Geophysics 46, 182–197. https://doi.org/10.1190/1.1441188.

Tournerie, B., Chouteau, M., Fox, L., Nagy, Z., 2000. Three dimensional magnetotelluric survey in Hungary. In: SEG Annual Meeting, Calgary. 2000.

Tuncer, V., Unsworth, M.J., Siripunvaraporn, W., Craven, J.A., 2006. Exploration for unconformity-type uranium deposits with audiomagnetotelluric data: a case study from the McArthur River mine, Saskatchewan, Canada. Geophysics 71, B201–B209.

Upadhyay, D., Chattopadhyay, S., Kooijman, E., Mezger, K., Berndt, J., 2014. Magmatic and metamorphic history of Paleoarchean tonalite-trondhjemite-granodiorite (TTG) suite from the Singhbhum craton, eastern India. Precambr. Res. 252, 180–190.

Verma, R.K., Rao, R.U.M., Gupta, M.L., 1966. Terrestrial heat flow in Mosabani Mine, Singhbhum District, Bihar, India. J. Geophys. Res. 71, 4943–4948.

Verma, R.K., Sarma, A.U.S., Mukhopadhyay, M., 1984. Gravity field over Singhbhum, its relationship to geology and tectonic history. Tectonophysics 106, 8797–93107.

Viljanen, A., 2012. Description of the magnetospheric/ionospheric sources. In: Chave, A.D., Jones, A.G. (Eds.), The Magnetotelluric Method: Theory and Practice. Cambridge University Press, Cambridge, pp. 96–121.

Vozoff, K., 1972. The magnetotelluric method in the exploration of sedimentary basins. Geophysics 37, 98–141.

Wannamaker, P.E., Wright, P.M., Zi-xing, Z., Xing-bin, L., Jing-xiang, Z., 1991. Magnetotelluric transect of Long Valley caldera: resistivity cross-section, structural implications, and the limits of a 2-D analysis. Geophysics 56, 926–940. https://doi.org/10.1190/1.1443126.

Wannamaker, P.E., 1999. Affordable magnetotellurics: interpretation in natural environments. Three Dimension. Electromagnet. 349–374. https://doi.org/10.1190/1.9781560802154.ch22.

Wannamaker, P.E., Hohmann, G.W., Ward, S.H., 1984. Magnetotelluric responses of three-dimensional bodies in layered earths. Geophysics 49, 1517–1533. https://doi.org/10.1190/1.1441777.

Weaver, J.T., Agarwal, A.K., Lilley, F.E.M., 2000. Characterization of the magnetotelluric tensor in terms of its invariants. Geophys. J. Int. 141, 321–336.

Weidelt, P., 1972. The inverse problem of geomagnetic induction. J. Geophys. 38, 257–289.

Yamaguchi, S., Ogawa, Y., Fuji-Ta, K., Ujihara, N., Inokuchi, H., Oshiman, N., 2010. Audio-frequency magnetotelluric imaging of the Hijima fault, Yamasaki fault system, southwest Japan. Earth Planets Space 62, 401–411. https://doi.org/10.5047/eps.2009.12.007.

Zhang, P., King, A., Watts, D., 1998. Using magnetotellurics for mineral exploration. In: SEG Technical Program Expanded Abstracts, 776-779, Society of Exploration Geophysicists, https://doi.org/10.1190/1.1820590.

Zhang, P., Chouteau, M., Mareschal, M., Kurtz, R., Hubert, C., 1995. High-frequency magnetotelluric investigation of crustal structure in north-central Abitibi, Quebec, Canada. Geophys. J. Int. 120, 406–418. https://doi.org/10.1111/j.1365-246X.1995.tb01828.x.